Aerosol chemistry, transport and climatic implications during extreme biomass burning emissions over Indo-Gangetic Plain

Nandita Singh[1], Tirthankar Banerjee[1,2], Made P. Raju[3], Karine Deboudt[4], Meytar Sorek-Hamer[5], Ram S. Singh[2,6] and Rajesh K. Mall[1,2]

[1]Institute of Environment and Sustainable Development, Banaras Hindu University, Varanasi, India
[2]DST-Mahamana Centre of Excellence in Climate Change Research, Banaras Hindu University, Varanasi, India
[3]High Altitude Cloud Physics Laboratory, Indian Institute of Tropical Meteorology, Pune, India
[4]Laboratoire de Physico-Chimie de l'Atmosphère, Université du Littoral Côte d'Opale, Dunkerque, France
[5]NASA Ames Research Center, Moffett Field, CA, USA
[6]Department of Chemical Engineering and Technology, Indian Institute of Technology (BHU), Varanasi, India

Correspondence to: Tirthankar Banerjee (tb.iesd@bhu.ac.in; tirthankaronline@gmail.com)

Abstract

The large-scale emissions of airborne particulates from burning of agricultural residues particularly over the upper Indo-Gangetic Plain (IGP) have often been associated with frequent formation of haze, adverse health impacts, modification in aerosol climatology and thereby aerosols impact on regional climate. In this study, short-term variations in aerosol climatology during extreme biomass burning emissions over IGP, and thereby to regional climate were investigated. Size-segregated particulate concentration was initially measured and submicron particles ($PM_{1.1}$) were found to dominate particulate mass within the fine mode ($PM_{2.1}$). Particulate bound water-soluble ions were mainly secondary in nature, primarily composed of sulfate and nitrate. There was evidence of gaseous NH_3 dominating neutralization of acidic aerosol species (SO_4^{2-}) in submicron particles, in contrast to crustal dominating neutralization in coarser particulates. Diurnal variation in black carbon (BC) mass ratio was primarily influenced by regional meteorology, while gradual increase in BC concentration was consistent with the increase in Delta-C, referring to biogenic emissions. Influence of biomass burning emissions were established using specific organic (levoglucosan), inorganic (K^+ and NH_4^+) and satellite-based (UV Aerosol Index, UVAI) tracers. Levoglucosan was the most abundant species within submicron particles (649 ± 177 ng m^{-3}), with a very high ratio (>50) against other anhydrosugars, indicating exclusive emissions from burning of agriculture residues. Spatio-temporal distribution of aerosol and few trace gases (CO and NO_2) were evaluated using both space-borne active and passive sensors. A significant increase in columnar aerosol loading (AOD: 0.98) was evident, with presence of absorbing aerosols (UVAI > 1.5) having low aerosol layer height (~1.5 km). A strong intraseasonality in aerosol cross-sectional altitudinal profile was even noted from CALIPSO, referring dominance of smoke and polluted continental aerosols across IGP. Possible transport mechanism of biomass smoke was established using cluster analysis and concentration weighted air mass back-trajectories. Short-wave aerosol radiative forcing (ARF) was further simulated considering intraseasonality in aerosol properties, which resulted in considerable increase of atmospheric ARF (135 Wm^{-2}) and heating rate (4.3 K day^{-1}) during extreme biomass burning emissions compared to non-dominating one (56 W m^{-2}, 1.8 K day^{-1}). Our analysis will be useful to improve understanding of short-term variation in aerosol chemistry over the IGP and to reduce uncertainties in regional aerosol-climate model.

1. Introduction

Aerosols are studied systematically in terms of their potential to influence the transfer of radiant energy and distribution of latent heat, by which it modifies the Earth's weather and climate. Aerosols are also associated with nutrient recycling and for governing atmospheric chemistry (Kanakidou et al., 2018). Aerosol interaction with radiation mainly constitutes its radiative forcing of climate change (Bellouin et al., 2005; Bond et al., 2013) while, it also modifies the climate by means of cloud formation processes (Seinfeld et al., 2016). The aerosol-radiation interaction necessitates understanding of spectrally varying aerosol optical properties, which are associated to particle size distribution, chemical composition, morphology and mixing states. The representation of aerosol processes in global/-regional climate models varies considerably and thereby, estimates of aerosol-radiation interaction still consist significant level of uncertainties (Myhre et al., 2013). This necessitates extensive regional investigation in terms of aerosol composition and properties for improved parametrization of aerosol schemes in the regional/-global climate model.

The Indo-Gangetic plain (IGP) in South Asia is especially unique in terms of aerosols loading and diversity that varies over the seasons (Singh et al., 2017a,b; Sen et al., 2017; Sayer et al., 2014; Kumar et al., 2018). The IGP is often projected to be one of the most vulnerable region in terms of aerosol induced negative health impacts (Apte et al., 2015) and therefore, numerous observational and modeling studies were made for better characterization of aerosols (Sen et al., 2017; Moorthy et al., 2008 and references therein). Recently, Singh et al. (2017a) has concluded the presence of spatial and seasonal variations in aerosol sources over South Asia, with vehicular emissions, followed by industrial emissions and secondary aerosols contributing most to fine particulates. Additionally, episode specific emissions like from biomass burning (Wan et al., 2017; Rajput et al., 2011, 2014; Rajput and Sarin, 2014) and use of fire crackers (Kumar et al., 2016) also induce sudden large-scale changes in aerosol properties and necessitate extensive investigation for better representation in regional aerosol model. Post-harvest agricultural residue burning, especially over upper IGP is projected to release 400 Gg of particulate bound organic aerosols (OA) and 40 Gg of black carbon (BC, Rajput et al., 2014), almost entirely (90 %) from burning of rice husks (Rajput et al., 2011). The OA mostly constitute the fine particulate mass (20-90 %) and are reported to be hydrophilic in nature (Rajput and Sarin, 2014) therefore, pose potential to act as CCN molecule, or at most compete with sulphate particles (Singh et al., 2017b). Nevertheless, presence of such huge amount of OA may either lead to a reduction in mean evaporation and modify regional precipitation or may reduce cloud formation processes by inducing additional heat to the system (Riipinen et al., 2011; Sun and Arriya, 2006). The biomass burning aerosols also impact the Earth's surface albedo by depositing on glaciers. The net radiative forcing of biomass burning aerosols by aerosol–radiation interactions is close to

neutral i.e. - 0.0 (-0.20 to + 0.20) W m^{-2}, having a gradient with negative forcing from OA and positive forcing from BC (Myhre et al., 2013). Biomass burning aerosols even evolve due to oxidation (Jimenez et al., 2009; Vakkari et al., 2014), from gas-phase precursors to semi-volatile secondary OA (SOA) and finally to highly volatile oxidized gases (e.g. CO and CO_2), thus warrants molecular characterization and specific understanding both in terms of composition, atmospheric chemistry, transport and radiative forcing (Singh et al., 2017b).

Several investigations were made over IGP to understand the characteristics of biomass burning aerosols. Few attempts were made solely using ground-based information e.g. aerosol emission budget (Rajput et al., 2014), organic mass-to-organic carbon ratio (Rajput and Sarin, 2014), emissions of PAHs (Rajput et al., 2011), organic molecular tracers (Wan et al., 2017; Li et al., 2014) and radiative forcing (Sharma et al., 2017; Alam et al., 2011); while few have explored remote sensing observations to interpret fire (Vadrevu et al., 2012) and aerosol plume characteristics (Kaskaoutis et al., 2014). However, there is a need to integrate both ground and contemporary satellite-based information so that spatio-temporal characterization of aerosols and its climatic impacts are assessed more realistically. In the present analysis complementary measurements from both ground and space-based platforms are therefore combined to trace the vital signatures of extreme biomass burning emissions, its chemical evolution, transport and aerosol radiative forcing. Initially, chemical speciations of size-segregated aerosols are made, supported by black carbon dynamics, molecular tracers of biomass emissions; and further explored in terms of their relevance to regional meteorology. The spatial extent of aerosol emission and transport was made using Modern-Era Retrospective Analysis for Research and Applications (MERRA) atmospheric reanalysis data, Global Data Assimilation System (GDAS) archives and NCEP/ NCAR Reanalysis data. Further, visualization from 'A-Train' satellite constellation, from both space-borne passive sensors like MODerate resolution Imaging Spectroradiometer (MODIS), Ozone Monitoring Instrument (OMI) and active sensor like Cloud-Aerosol Lidar and Infrared Pathfinder Satellite Observation (CALIPSO) are included. Briefly, the results are explored to highlight three exclusive but inter-related mechanisms, i.e. aerosol chemistry, regional transport and radiative forcing, and their intra-seasonal variations over middle IGP, which may well be useful in regional climate model.

2. Experimental methods

2.1 Site description

Ground-based aerosol measurements were made at the institutional premises of Banaras Hindu University, Varanasi (25.26 °N, 82.98 °E, 82 m AMSL). The ground station typically experiences a humid sub-tropical climate, with no localized effects of oceans or mountains (Fig. 1). The

1 predominating wind profile is north-westerly which are projected to subsidize over a section of middle

2 IGP, coinciding well with the ground monitoring station, thereby facilitates gradual accumulation of

3 aerosols (Kumar et al., 2018). Interestingly enough, the region also experiences a significant diurnal

4 variation in atmospheric boundary layer (ABL) associated with high convective turbulence that usually

5 redistribute aerosols to a greater height (Kumar et al., 2015a,b, 2017a). Particulates emitted from

6 crustal sources, road dust re-suspension, vehicular exhausts and biomass/waste burning are often

7 reported to constitute the regional aerosols (Singh et al., 2017a).

8 **2.2 Micro-meteorology, ABL and wind field**

9 The 24 h average meteorological parameters e.g. temperature, relative humidity (RH) and

10 wind speed (WS) were obtained from wunderground.com and validated with regional weather

11 monitoring station data. The ABL heights at specific coordinate were retrieved from Global Data

12 Assimilation System (GDAS) archives hosted at NOAA-Air Resource Laboratory, which provides

13 simulated meteorological observations at a gridded scale. The 3-hourly ABL data (0.5°) were averaged

14 on daily basis in parallel to period of particulate measurement. The NCEP/NCAR Reanalysis data was

15 used to analyze the variation of 3-D wind fields at near surface (1000 m) with a horizontal resolution

16 of 2.5° X 2.5°. Vector wind composite mean (m s^{-1}) for 925 hPa was plotted for the defined coordinate

17 (6-38 °N, 50°-105 °E) to understand the synoptic pattern of wind field.

18 **2.3 Ground-based measurements**

19 2.3.1 Size-segregated aerosol mass concentration

20 Size-segregated aerosols were collected on pre-combusted quartz fiber filter using Anderson

21 eight-stage cascade impactor (Tisch Environmental Inc., USA). Sampling was continued for once in a

22 week from 1st October to 15th December 2016, continuously for 72 h (in each week) to get

23 representative deposition of particulates. The instrument was run with a fix flow rate of 28.3 LPM,

24 having aerodynamic cut-off diameter of <0.43, 0.65, 1.1, 2.1, 3.3, 4.7, 5.8 and >9.0 μm (with 50 %

25 collection efficiency). The individual stages of each sample were then segregated into three groups on

26 the basis of cut-off diameter (i) coarse mode (PM$_{>2.1}$) comprising the stages with the aerodynamic

27 diameter >2.1 μm; (ii) fine mode (PM$_{1.1-2.1}$) for the stages with diameter 1.1 to 2.1 μm; and (iii)

28 submicron mode (PM$_{<1.1}$) for the last two stages with the diameter <1.1 μm.

29 2.3.2 Black carbon mass concentration

30 The black carbon (BC) real-time mass concentration was measured using a seven channel

31 Aethalometer (Model AE-42; Magee Sci. Inc., USA), with a constant flow rate of 3 LPM at 5 minutes

32 resolution. Aethalometer measures the attenuated beam of light transmitted through aerosol sample

on filter tape at seven wavelengths (370, 470, 520, 590, 660, 880 and 950 nm), while attenuation at 880 nm was considered for BC (Bodhaine, 1995). The BC concentration is estimated based on the concept of linearity between the light attenuation and BC mass deposited on quartz filter. An absorption efficiency of 16.6 $m^2\,g^{-1}$ (provided by the manufacturer) was used to measure BC after correction of loading effect. The mechanism for estimation of BC is described in Wang et al. (2011) and Kumar et al. (2017a). BC measured at two wavelengths e.g. 370 nm (indicating absorption by wood-smoke particles) and 880 nm (by both fossil fuel and wood burning emissions) were used to compute Delta-C ($BC_{370nm} - BC_{880nm}$). Delta-C is reported to symbolize smoke emissions (Wang et al., 2011; Kumar et al., 2016) and therefore, was used as a tracer for biomass emissions.

2.3.3 Aerosol chemical constituents

Water-soluble ions

The particulate deposits on filter were extracted with deionized water in an ultrasonic bath (Microclean-109, Oscar, India) for 30 min, and extracts were further filtered through syringe filters (pore size 0.2 μm). The water-soluble ionic constituents (WSIC) were analyzed by ion exchange chromatograph (ICS 3000, Dionex, USA). For measurement of anions (Cl^-, NO_3^-, SO_4^{2-} and PO_4^{3-}), the IC was equipped with a micro-membrane suppressor (AERS-300, 4 mm; Dionex) with IonPac analytical column (AS11-HC × 250-mm) connected with a guard column IonPac (AG11-HC, 4×50mm; Dionex). Cations (NH_4^+, Na^+, K^+, Mg^{2+}, Ca^{2+}) were measured through a suppressor (CERS-300, 4 mm; Dionex) with an analytical column (IonPac CS12A-HC, 4×250 mm; Dionex) and a guard column (IonPac CG11-HC, 4 × 50 mm; Dionex, USA). The background contamination was removed by subtracting the blank filter value from sample values (Kumar et al., 2017b).

Trace metals

The trace metals were extracted from filter discs as per US EPA Method IO-3.2 (EPA, 1999). The filters were cut into pieces and digested in acid mixture solution (5.55 % HNO_3 with 16.67 % HCl) on a hot plate for 2 h. The extracts were filtered, stored at 4 °C and were analyzed by atomic absorption spectrophotometer (Avanta Ver 2.01, GBC) for Ca, Na, K, Cu, Mn, Fe, Cd, Cr, Pb, Ni, Co, and Zn.

Organic compounds

For determining the aerosol organic constituents, the filter composites of each group were extracted by ultrasonicating the filters initially with dichloromethane-hexane mixture (1:1), followed by dichloromethane-methanol mixture (1:1). Both solvent extracts were combined and concentrated using vacuum rotatory evaporator and nitrogen evaporator to a volume of 100 μL (Hu et al., 2013).

The extracts were derivatized by silylation with N, O-bis-(trimethylsilyl)-trifluoroacetamide and 1 % trimethylchlorosilane prior to analysis. After derivatization, the residue was re-dissolved in hexane and analyzed by gas chromatography-mass spectrometry (GCMS-QP2010 Ultra, Shimadzu, Japan) equipped with Rxi-5MS fused silica capillary column having dimension 30 m x 0.25 mm id x 0.25 µm (Restek, Bellefonte, PA, USA). Sample was injected in GCMS at 260°C injector temperature in splitless mode. The column oven temperature program was started at 50°C with 2 min of the isothermal hold which further raised up to 120 °C (linear elevation @ 30 °C min^{-1}) and 300 °C (linear elevation @ 6 °C min^{-1}) followed by the isothermal hold of 11 min. The electron impact ionization was used to produce molecular ions at 70 eV with the ion source and interface temperature of 230 °C and 270 °C, respectively. The molecular ions were scanned for a wide range of m/z from 40 to 650. The target compounds were identified based on retention time and fragmentation pattern from National Institute of Standards and Technology (NIST) library and standard solutions of analytes. The average recoveries (respective RSD) of the n-alkanes (28 compounds) varied from 72-92% (1-12%), 75-88% (2-7%) for phthalates (6 compounds), 74-92% (1-9%) for FAMES, 73-93% (1-10%) for PAHs and 75-80% (4-6%) for anhydrosugars (3 compounds).

2.4 Satellite-based observations

2.4.1 Aqua/-Terra MODIS data

The aerosol optical depth (AOD) at 550 nm was retrieved daily from MODIS onboard Aqua satellite in parallel to ground-based aerosol monitoring. The level 2 Collection 6 AOD at 10 km resolution was retrieved using MODIS merged DT-DB AOD (AOD_550_-Dark_Target_Deep_Blue_Combined, Levy et al., 2013). The selection of merged DT-DB for retrieving AOD was based on higher retrieval number and accuracy across the IGP (Mhawish et al., 2017). The AOD over the ground station was calculated as the average of 5 x 5 pixels, surrounding the monitoring site. Angstrom exponent (AE, α) was retrieved using MODIS C6 level 2 DB AOD and relation between AOD and AE was used to measure the aerosol loading and the particle size (Kumar et al., 2015a; Mhawish et al., 2017). Columnar water vapor content (CWV) was retrieved from Aqua MODIS collection 6 level 2 infrared channel at 1 km spatial resolution. To illustrate the impact of biomass burning, the fire spots were retrieved over the IGP from Aqua/-Terra MODIS Fire Mapper product (collection 6, spatial resolution 1×1 km^2) provided by the Fire Information for Resource Management System (FIRMS, https://firms.modaps.eosdis.nasa.gov). Details about MODIS fire products and its algorithm may be found elsewhere (Justice et al., 2006).

2.4.2 Aura-OMI and MERRA-2 reanalysis data

The OMI onboard AURA satellite has a typical daily global coverage with 13×24 km^2 spatial resolution at nadir and measures solar backscatter irradiation in the UV–visible spectrum (264-504 nm; Levelt et al., 2006). Ultraviolet Aerosol Index (UVAI), tropospheric NO_2, total columnar ozone (TCO) and Single scattering albedo (SSA) were retrieved from Aura OMI available at NASA Goddard Earth Sciences Data and Information Services Centre (GES DISC). Aura OMI UVAI is capable of detecting aerosol absorption from satellite measured radiances without any prior assumption on aerosol composition (Torres et al., 2013). It is a qualitative parameter and is widely used to identify the UV absorbing aerosols (e.g. smoke plumes, soot and mineral dust; Torres et al., 2013; Mhawish et al., 2018). The UVAI based on OMI near-UV aerosol retrieval algorithm (OMAERUV) was extracted from Level 2G, version 003 aerosol product containing one day's Level 2 data set of original pixels (13×24 km^2) into 0.25° x 0.25° grids. The NO_2 tropospheric column density was retrieved from cloud screened (cloud fraction <30 %) Level 3, version 003, daily 0.25° x 0.25° gridded OMNO2d product (Krotkov et al., 2017). To estimate TCO, Level 3e data (OMDOAO3) at a spatial resolution of 0.25° x 0.25° was used. SSA at 550 nm was retrieved from OMI level 2G product (OMAERUV) at 0.25° × 0.25° resolution. The Carbon Monoxide (CO) surface concentration (in ppbv) was retrieved from Modern-Era Retrospective Analysis for Research and Applications, version 2 (MERRA-2) atmospheric reanalysis data available at 0.5° x 0.625° from GES DISC.

2.4.3 CALIPSO-CALIOP observations

CALIPSO products were used to examine the vertical distribution of aerosols, altitude of aerosol layers, clouds, aerosol types and their properties at visible (532nm) and near-IR wavelengths (1064 nm). The V4.10 CALIOP Level 2 altitude-orbit cross-section profiles obtained from CALIPSO sub-setting web application (https://www-calipso.larc.nasa.gov) was used. The Lidar profiles were processed for images of vertical feature masks, aerosol subtypes and extinction coefficients (at 532 nm) at 30 m vertical resolution over the selected grid (80°-86 °N and 22°-28 °E). Details about data products, calibration and uncertainty are discussed in Rogers et al. (2011).

2.5 Air-mass back trajectory

The NOAA HYSPLIT model (Draxler and Rolph, 2003) was used to simulate particle back trajectories in a three-dimensional system. The HYSPLIT was run on using the Global Data Assimilation System data (GDAS, 0.5°×0.5°) available from archive dataset (http://ready.arl.noaa.gov/gdas1.php) to predict 120 h air-mass back trajectories (00:00, 06:00, 12:00 and 18:00 UTC) starting from October to December 2016. Trajectories for different aerosol loading periods were then overlaid on MODIS fire map to study the transboundary movement of emissions from biomass burning. The trajectory analysis was made using GIS-based software TrajStat (Wang et al., 2009). Concentration weighted

trajectories (CWT) were also drawn considering columnar aerosol loading to evaluate potential aerosol source fields and mechanism of aerosol transport. The specificities of the models' parameters and algorithms are detailed elsewhere (Wang et al., 2009; Kumar et al., 2018).

2.6 Aerosol optical properties, radiative forcing and heating rate

Aerosol induced shortwave (0.2–4.0 µm) direct radiative forcing (ARF) was estimated using Santa Barbara DISORT Atmospheric Radiative Transfer (SBDART) model (Ricchiazzi et al., 1998). The SBDART estimates plane-parallel radiative transfer in a clear sky condition for both Earth's top of the atmosphere (TOA) and at the surface (SUF), while atmospheric forcing (ATM) is calculated as the difference between them. The standard atmospheric profile is used together with input variables e.g. AOD, SSA, CWV, TCO and asymmetry parameter (ASP) derived through OPAC model (Optical Properties of Aerosols and Clouds; Hess et al., 1998). The OPAC provides aerosol optical properties over a wide range of wavelength and delivers necessary input to SBDART. Mean mass concentrations of aerosol water soluble (WSIC) and insoluble (dust and organics) components along with BC mass concentration were converted to particle number densities and introduced to OPAC to derive aerosol optical properties. The AOD and SSA were reconstructed to match modelled and satellite derived values within ±5 % deviation.

The weekly mean values of AOD, SSA, ASP, CWV, TCO, visibility and AE were included as inputs to SBDART. The SBDART includes multiple scattering in a vertically inhomogeneous, non-isothermal plane-parallel media, and is reported to be efficient in resolving the radiative transfer equation (Raju et al., 2016). The ARF was calculated using 10 solar zenith angles (0 to 89, with increment of 10) and was proceed for conditions like 'with aerosols' or 'without aerosols'. The surface albedo was decided based on visual observation considering a combination of snow, ocean, sand and vegetation. Overall uncertainty in the estimated ARF was in the range of 10–15 % (Alam et al., 2011). The ATM-ARF was further used to compute atmospheric heating rate ($\partial T/\partial t$, K day^{-1}), using equation (1):

$$\partial T/\partial t = (g/Cp)*(\Delta F/\Delta P) \tag{1}$$

where ΔP is the difference in forcing, ΔP is the pressure difference between top and bottom boundary layer, *Cp* is specific heat capacity of air at constant pressure and *g* is the acceleration due to gravity (Kumar et al., 2017a).

3. Results and discussion

3.1 General characteristics of aerosols

The weekly variation in particulate concentrations in different size fractions are presented in Fig. 2 with the descriptive statistics included in Table S1. The total aerosol mass concentration have

high intra-seasonal variations (median: 370; range: 134-734 $\mu g\ m^{-3}$), mainly influenced by coarse mode particles ($PM_{>2.1}$) contributing 63±15 % of particulate mass. In contrast, contribution of submicron ($PM_{<1.1}$: 27±12 %) and fine mode particles ($PM_{1.1-2.1}$: 10±4 %) to total aerosol loading were relatively less (<37%). The average (±1σ) mass concentration of $PM_{2.1}$ ($PM_{<1.1} + PM_{1.1-2.1}$) and total aerosol loading was 162 (±123) and 390 (±199) $\mu g\ m^{-3}$, which were approximately 98 % (against $PM_{2.5}$) and 92 % higher compared to annual averages observed over the monitoring station (Murari et al., 2017; Prajapati and Tripathi, 2008). To our knowledge, till the submission of the manuscript, there was no published report on submicron particle over the ground station. Time-series analysis of size-segregated particulates (Fig. 2) indicate the submicron ($PM_{<1.1}$) and fine mode particles ($PM_{1.1-2.1}$) only had a late rise in mass concentration, while the coarse mode particulates ($PM_{>2.1}$) did not show any trend. However, there was a definite increasing pattern in fine to coarse particle ratio ($PM_{2.1}/PM_{>2.1}$; mean: 0.7±0.5; range: 0.2-1.5), due to a continuous increase of the fine mode from mid-November to the end of the monitoring. Thus, the contribution of fine mode particle to total aerosol loading increased from mid-November (>40 %), and contributed almost 60 % of particulate mass during the month of December. The submicron particles also indicate a high median concentration (96 $\mu g\ m^{-3}$) compared to fine mode (33 $\mu g\ m^{-3}$), and the particle ratio ($PM_{<1.1}/PM_{1.1-2.1}$) remain >1 throughout, only to exceed values >2.5 from November to December. This clearly indicates the dominance of submicron particles within fine mode fractions, possibly associated to anthropogenic emissions, and also influenced by local meteorological conditions e.g. low temperature (mean±SD: 20±3 °C), calm wind (mean: 0.6 m s^{-1}) and shallow boundary layer height (mean±SD: 379±89 m).

3.2 Aerosol chemical speciations

3.2.1 Water soluble inorganic species (WSIS)

Temporal variation of WSIS in size-segregated airborne particulates are presented in Fig. 3a. It indicates the major contribution of WSIS to submicron (21 %) and fine particle mass (21 %) compared to the coarser one (13 %). The secondary inorganic aerosols (SIA = SO_4^{2-} + NO_3^- + NH_4^+) together accounted for 17 % of the submicron particle mass, with major contributions from sulfate (9%) and nitrate (6 %). Similar was the case for fine particulates as SIA contributed to almost 17 % of aerosol mass with predominate contribution from sulfate (8 %) and nitrate (6 %), and a relatively small proportion of ammonia (4 %). In contrast, the relative contribution of SIA to coarse particulate was lower (7 %), also primarily associated to sulfate (5 %) and nitrate compounds (2 %). This indicates the secondary nature of origin of fine and submicron particles which possibly evolve through gas-phase photochemical conversion of SO_2 and NO_2, eventually neutralized by crustal species like carbonate salts ($CaCO_3$ and $MgCO_3$) associated with the airborne dust. The time-series of SIA contribution to

1   particulate mass (Fig. 3a) indicate a dominance (although in different extent) of secondary aerosols in

2     $PM_{1.1-2.1}$ and $PM_{>2.1}$ only during November.

3   Among the WSIS, SO_4^{2-} was invariably the most abundant species within each particulate size

4   fraction ($PM_{<1.1}$: 39 %, $PM_{1.1-2.1}$: 32 %, $PM_{>2.1}$: 36 %), followed by NO_3^- ($PM_{<1.1}$: 27 %, $PM_{1.1-2.1}$: 29 %,

5     $PM_{>2.1}$: 17 %). The NO_3^- / SO_4^{2-} ratio was considered as an indicator of the mobile and stationary source

6   contribution to nitrogen and sulfur (Tian et al., 2016). An average ratio varying from 0.62 to 1.92 was

7   noted for all size-segregated particulates testifying dominance of both sources, although in different

8   time-scales. In later phase, the ionic ratio (NO_3^- / SO_4^{2-}) enhanced (>1) in submicron and fine mode

9   particles, well identical to the reported haze events over Guangzhou (Tan et al., 2009) and Suzhou,

10   China (Tian et al., 2016). A very high NO_3^- / SO_4^{2-} ratio (3.2±1.3) was only noted in fine aerosols during

11   October, mainly due to lower concentration of sulphate. The next two dominant contributors to WSIS

12   were NH_4^+ ($PM_{<1.1}$: 14 %, $PM_{1.1-2.1}$: 19 %, $PM_{>2.1}$: 5 %) and K^+ ($PM_{<1.1}$: 8 %, $PM_{1.1-2.1}$: 5 %, $PM_{>2.1}$: 2 %),

13   both considered as a molecular tracer for biogenic emission (Banerjee et al., 2015). They constitute

14   the greater proportion of WSIS in $PM_{<1.1}$ and $PM_{1.1-2.1}$, especially from last week of October till the end

15   of November, signifying elevated contribution of biomass/ agro-residue burning emissions to these

16   particle sizes. Further, a strong correlation (R^2=0.9) between NH_4^+ and SO_4^{2-} and high NH_4^+/SO_4^{2-}

17   equivalent ratio (0.9±0.2) for submicron particulates indicate the abundance of gaseous NH_3 to

18   neutralize acidic species (SO_4^{2-}) by forming $(NH_4)_2SO_4$ and/or NH_4HSO_4. The NH_4^+/SO_4^{2-} equivalent ratio

19   gradually increased from week 5 (mean: 1.2, range: 0.9-1.3), possibly due to abundant emission of

20   NH_4^+ from biomass emissions. Unlike submicron particles, the low NH_4^+/SO_4^{2-} equivalent ratios (<0.7,

21   mean: 0.4) in coarse mode particles indicate the predominant neutralization by crustal minerals.

22   Unlike the other WSIS, Na^+ and Ca^{2+} were found to contribute maximum in $PM_{>2.1}$ (Na^+: 2 %;

23   Ca^{2+}: 3 %), referring their crustal origin. The relative abundance of Cl^- in size-segregated aerosols was

24   roughly equal for each size fraction, contributing almost in identical to total WSIS in $PM_{<1.1}$ (6 %), $PM_{1.1-2.1}$

25   (5 %) and $PM_{>2.1}$ (4 %). The possible origin of Cl^- in $PM_{>2.1}$ could be the aged sea salt, transported

26   from Bay of Bengal, but its association with $PM_{<1.1}$ was most likely due to biomass burning emissions

27   (Pavuluri at al., 2011; Murari et al., 2015). The temporal variations of WSIS in all particulate size

28   fractions were consistent except for Mg^{2+} and PO_4^{3-} contributing <0.2 % of particulate mass and having

29   non-biomass specific emission sources. A strong correlation between the anion and cation equivalents

30   within all the size groups (0.7-0.9) indicate that the most ions were from the filter samples. The total

31   ion equivalent ratio (anions to cation) refer a cationic imbalance ($PM_{<1.1}$: 1.2, $PM_{1.1-2.1}$: 0.8 and $PM_{>2.1}$:

32   0.6) with excess cations in fine and coarse mode particles, possibly due to unmeasured components

33   like carbonates and bicarbonates.

34   *3.2.2 Trace metals*

Total metallic contribution to particulate mass was found maximum in $PM_{1.1-2.1}$ (24 %), followed by $PM_{>2.1}$ (11 %) and least in $PM_{<1.1}$ (7 %, Fig. 3b). The most abundant elements were Na, Ca, K and Zn for all size fractions, contributing 90-98 % of total identified metals, while the remaining fractions were primarily constituted by Fe (1-10 %). Within the detectable level of metals, Ca and Na share 88 % of metal concentrations in $PM_{<1.1}$ and 7% of submicron particulate mass, without having any specific temporal trend. However, Ca, Na were found high in $PM_{1.1-2.1}$ (Ca: 10 %; Na: 7 %), referring their origin from resuspension of crustal materials and road dust.

There are few evidences of trace metal emissions from burning of biomass. Wang et al. (2015) have concluded biomass combustion as the most prominent source of Fe concentration in submicron particles. For this analysis, although Fe was measured maximum in $PM_{>2.1}$, the relative increase in Fe concentration in submicron ($PM_{1.1}$: 59 %) and fine aerosols ($PM_{1.1-2.1}$: 415 %) during week 6 to week 9 possibly indicate the added contribution of biomass burning emissions. Beside Fe, there are also reports of trace metals emissions particularly K, Cu, S, Zn, Pb from burning of rice-straw (Ryu et al., 2012); organic bound Fe^{2+}, Cu^{2+}, Ni^{2+}, Zn^{2+} from hardwood burning (Chang-Graham et al., 2011) and Cu, Pb, Ni, As from the burning of biomass fuel (Zhang 2014). In our case, massive increase in K ($PM_{1.1}$: 528 %; $PM_{1.1-2.1}$: 119 %) was also noted between week 6 and week 9. This contrasted with coarse particle bound Fe and K which are primarily of crustal origin (Banerjee et al., 2015), and recorded only 15 % (Fe) and 83 % (K) increase in concentration within week 6 to 9. Zinc was found considerably high in $PM_{>2.1}$ (3 %) and relatively small proportion in $PM_{1.1-2.1}$ (2 %). The major sources of atmospheric Zn are burning of residual oil, refuse and garbage (Gonzalez et al., 2016) which possibly leads to higher mass fractions in coarser particulates. Here, a relatively high Zn concentration was noted in later phase of monitoring irrespective of particulate size coincide with the winter specific burning of waste/-refuse over the region (Kumar et al., 2017b). The relative contribution of rest of the trace metals (e.g. Mn, Pb, Cd, Ni, Cu, Cr and Co) to particulate mass were insignificant (<0.05 %), without having any specific temporal pattern.

3.3 Characteristics of BC mass loading

Daily means of BC concentration and Delta-C ($BC_{370} - BC_{880}$) are plotted in Fig. 4 with some data gaps. The 24 h average BC concentration varied from 2.0-15.4 µg m^{-3} with a seasonal mean (±1σ) of 8.3 (±2.9) µg m^{-3}. The season specific BC average was 80 % higher in comparison to annual mean (4.6 µg m^{-3}; Kumar et al., 2017a), while there were also reports of winter-specific very high BC concentration (22 µg m^{-3}; Murari et al., 2016) that usually persist over the region. A distinct diurnal profile with high BC concentration during nighttime (>9 µg m^{-3}; 11:00-7:00 h) and low daytime concentration (<6 µg m^{-3}, 11:00-17:00 h) was also noted. Gradual rise in BC mass loading from 17:00 h could be mainly attributed to the regional meteorology which is reported as the most influential

factor in regulating BC concentrations compared to the anthropogenic sources (Kumar et al., 2015b, 2017a). Regional meteorology, particularly boundary layer height and transport are two fundamental processes that influence the diurnal BC variation, mainly by means of regulating horizontal and vertical transport (Kumar et al., 2015b). Therefore, the diurnal variation in BC concentration were the consequence of change in boundary layer height with occasional inflow of emissions from large-scale burning of agriculture residues/ biomass/ waste and from vehicular emissions.

The BC timeseries shows an enhanced BC concentration from the end of October (week 4) till the November end (week 9). Such increase in BC concentration was however, possibly due to increased source strength as there was no significant variation in meteorological variables (like ABL) within this timeframe (Table S1). To understand the variation in BC sources, 24 h average Delta-C concentration (mean±SD: 2.3 ± 1.0 µg m^{-3}) is also included in Fig. 4, which refers the emission of smoke particles (Wang et al., 2011; Kumar et al., 2016). Except few exceptions, high Delta-C (>2.3 µg m^{-3}) was observed particularly in the month of November (80 % of days) compared to October (23%) and December (46 %), referring added contribution of biomass burning emissions.

3.4 Composition of organic aerosols

Size-segregated particle-bound organic aerosols (OA) were analysed for 22 *n*-alkanes (C_{13}-C_{34}), 3 anhydrosugars (levoglucosan, mannosan and galactosan), 4 PAHs and 10 *n*-alkanoic acids (C_{12}-C_{26}) (Fig. 5). Considerable variation in the concentration and size distributions of these OA were noted. Contributions of OA to size-segregated particulates were relatively less because of partial characterization through GC-MS. Among the identified species, *n*-alkanes were invariably the highest within PM$_{<1.1}$ (mean±SD: 484 ± 103 ng m^{-3}) compared to fine (267 ± 43 ng m^{-3}) and coarse mode aerosols (308 ± 93 ng m^{-3}). The molecular distribution of *n*-alkanes homologues in all three size fractions showed a slight dominance of odd-numbered *n*-alkanes. The CPI (Carbon Preference Index) remain close to unity (CPI range: 1.2-2.1; mean±SD: 1.5 ± 0.5), indicating dominance of anthropogenic emissions like combustion of fossil fuels and biomass burning. The higher molecular weight homologues (>C_{25}) concentration were found highest in PM$_{<1.1}$ with an oscillating pattern, having odd molecules concentration higher than the adjacent even molecules (Fig. 5b). In contrast the low molecular weight homologues (<C_{25}) showed no such specific pattern of odd/even dominance. The sources of higher homologues (C_{27}, C_{29} and C_{31}) are probably the surface deposited plant litter for coarse mode and biomass burning for fine mode aerosols, while low molecular weight homologues (<C_{25}) primarily originate from the fossil fuel combustion (Kang et al., 2016). Saturated fatty acids were found to constitute a larger fraction of solvent extractable organics within coarse mode (439 ± 38 ng m^{-3}) and submicron particles (357 ± 162 ng m^{-3}) in comparison to fine mode (171 ± 57 ng m^{-3}). For all three size fractions, total low molecular weight fatty acids (≤C_{20}) concentration was found higher than the

high molecular weight fatty acids ($\geq C_{20}$), indicating the anthropogenic emissions like vehicular, residential biomass burning and energy practices. Presence of high concentration of C_{12}, and C_{15} refer the dominance of cooking oil combustion. The high concentration of C_{22} further suggests the influence of biomass burning which potentially emit both, high and low fatty acids (Mochida et al., 2007). The fatty acid amide was found in trace amount which could possibly be derived from fatty acid and ammonia during burning process. Presence of PAHs was also measured for size-segregated particulates and was found highest in submicron particulates (7.0 ng m^{-3}) compared to PM$_{1.1-2.1}$ (3.6 ng m^{-3}) and PM$_{>2.1}$ (3.1 ng m^{-3}). PAHs are mainly produced due to incomplete combustion of fuels like fossil fuels and biomass at relatively high temperature (Singh et al., 2017b; Chen et al., 2015). There was no previous report of submicron particulate bound PAHs during biomass burning emissions over IGP to compare, except for PM$_{2.5}$ bound PAHs in Patiala (27-40 ng m^{-3}; Rajput et al., 2011, 2014), Agra (9 ng m^{-3}; Villalobos et al., 2015), Kanpur (3 ng m^{-3}; Villalobos et al., 2015) and total aerosol bound PAHs in Kathmandu (320 ng m^{-3}, Chen et al., 2015).

Levoglucosan was found to be the most abundant anhydrosugar in submicron particles with an average ($\pm 1\sigma$) of 649 (± 177) ng m^{-3}. In contrast, concentration in fine (229$\pm$87 ng m^{-3}) and coarse particles (162$\pm$68 ng m^{-3}) were relatively low, referring the influence of biomass burning emissions for submicron particles. Levoglucosan concentration measured in this study are well comparable to other reported observations, especially with the cases that have accounted the influence of biomass burning emissions e.g. New Delhi (1978 ng m^{-3}, Li et al., 2014), Mt. Tai, China (391 ng m^{-3}, Fu et al., 2008), Gent, Belgium (477 ng m^{-3}, Zdrahal et al., 2002), Lumbini, Nepal (734 ng m^{-3}, Wan et al., 2017) and Beijing, China (590 ng m^{-3}, Cheng et al., 2013). Beside levoglucosan, relative concentration of other anhydrosugars (mannosan and galactosan) in all size-segregated aerosols were negligible (<70 ng m^{-3}, not shown).

3.5 Signature of biomass burning emissions

Biomass primarily consists of different bio polymers (e.g. cellulose, hemicellulose, lignin, suberin, sporopollenin and chitin) with small proportion of lipids and terpenoids. During thermal combustion, such biomass emits different types of organic molecules, some of which have the potential to be considered as signature molecule based on their long residence time and chemical stability (Banerjee et al., 2015). The major combustion product of cellulose and hemicellulose includes anhydrosugars like levoglucosan (1,6-anhydro-β-D-glucopyranose, $C_6H_{10}O_5$) and its two isomers (mannosan and galactosan). Among these, levoglucosan is a robust and widely used tracer for biomass burning emissions, both globally (Simoneit et al., 1999; Schkolnik et al., 2005; Cheng et al., 2013), and over IGP (Li et al., 2014; Banerjee et al., 2015; Wan et al., 2017). In our case, levoglucosan was abundant in submicron particles with a peak during November (week 6 to 9, Fig. 6). The rise in

concentration was universal in each particulate size fractions, but typically in submicron (837±83 ng m^{-3}) and fine particulates (311±47 ng m^{-3}), having 54-70 % rise against rest of the monitoring period. This could correspond to a short-term variation in emissions source strength which possibly well influenced the aerosol property. A ratio between levoglucosan with rest of the anhydrosugars (mannosan and galactosan) was also considered to indicate the dominating type of biomass burning, with a ratio <10 specific for softwood combustion, and >10 for burning of hardwood and crop residues (Cheng et al., 2013). Even a ratio >40 was reported from physical experiments using rice straw, wheat straw and maize stalks (Engling et al., 2009). Although, the presence of mannosan and galactosan was not frequent in our case, but an overall ratio >50 refers the exclusive dominance of agriculture residue burning across the IGP.

The possibility of considering K^+ and NH_4^+ as biomass burning tracers were investigated in terms of their association with levoglucosan for submicron and fine particulates. In general, the temporal trend of levoglucosan coincided well with both K^+ and NH_4^+, and all these tracers registered a gradual rise in concentration during November. Highly significant correlation (R^2) between levoglucosan and K^+ ($PM_{1.1}$: 0.80, $PM_{1.1-2.1}$: 0.76; $p<0.01$), and levoglucosan and NH_4^+ ($PM_{1.1}$: 0.95, $PM_{1.1-2.1}$: 0.60; $p<0.01$) were noted at 99 % confidence interval. That definitely indicates that levoglucosan, K^+ and NH_4^+ have similar biogenic sources over IGP which predominately contribute to the aerosol loading, especially in $PM_{1.1}$ and $PM_{1.1-2.1}$. The relation between levoglucosan with K^+ and NH_4^+ further appeared to be non-linear, with an exponential fit for submicron (R^2: 0.84, 0.94) and for fine particulates (R^2: 0.83, 0.65). Non-linear correlations between levoglucosan and K^+ are also reported at Amazon (Schkolnik et al., 2005) and in Beijing (Cheng et al., 2013) during extreme biomass burning emissions. There was also evidence that NH_4^+ was better associated with levoglucosan compared to K^+, referring the presence of additional K^+ sources across the region (like fireworks, Kumar et al., 2016). However, in absence of aerosol organic carbon content, contribution of biomass burning to aerosol mass was not computed.

Besides using conventional biomass burning tracers, we also evaluated the association of submicron and fine particulate bound levoglucosan with weekly averages of Delta-C and UVAI (Fig. 6). Both Delta-C and UVAI are the measures of identifying the relative dominance of absorbing aerosols. In all scenarios, significant correlation (R^2) was noted between levoglucosan with Delta-C (0.65, $p<0.01$) and UVAI (0.66, $p<0.01$). In addition to the ground-based aerosol measurement, dynamic profile of trace gases concentration, especially for those that behave as aerosol precursors, are assessed from Real-time Air Quality Data inventory of Central Pollution Control Board (https://app.cpcbccr.com/ccr). The hourly average concentrations of individual trace gases were initially checked for data quality and outliers, and further averaged to 24 h. No such universal trend in

1 concentration of all the trace gases was evident, except an overall increasing trend for NO, NO_2, NOx,

2 and CO, while SO_2 remained stable and there was a negative trend for O_3. The most striking feature

3 was to have an increase in concentration particularly during November, although of different

4 magnitude. This was also evident in the variation of particulate bound biomass tracers, which inspire

5 us to consider two different aerosol loading scenarios *viz*. scenario 1 for biomass burning dominating

6 period (week 6 to 9, BDP) and scenario 2 for biomass burning less dominant period (week 1-5 and

7 week 10-11, BLDP). Such classification was intended to recognize if there was any variation in aerosol

8 source fields over IGP and in aerosol-induced radiative forcing.

9 **3.6 Spatio-temporal nature of aerosol columnar properties**

10   Spatio-temporal variations in aerosol columnar properties and trace gases are plotted in Fig.

11 7a, including the daily variations at the ground station (Fig. 7b). Instead of considering the columnar

12 properties for the entire season, spatial plots are generated for two different scenarios like BDP and

13 BLDP.

14   The spatial pattern in aerosol columnar properties was typical having a very high aerosol

15 loading exclusively over IGP (area weighted AOD mean±SD: 0.55±0.21) in comparison to the rest of

16 South Asia (0.31±0.21). However, there was no such temporal variation particularly over IGP as both

17 BDP_{AOD} (0.56±0.23) and $BLDP_{AOD}$ (0.53±0.23) was almost similar. The BDP_{AOD} was slightly higher (12 %)

18 to that of reported decadal average (0.50±0.25, Kumar et al. 2018), and was comparable to the season

19 specific average over IGP (0.55±0.20; Kumar et al., 2018). It should be noted that area weighted AOD

20 average includes all the pixels retrieved across the region, some of which may not represent the

21 biomass emissions. This leads us to further retrieve and compare AOD particularly over the ground

22 station. In this case, the mean AOD was significantly high during post-monsoon (0.81±0.39), 44 %

23 higher for BDP_{AOD} (0.98±0.42) in respect of $BLDP_{AOD}$ (0.68±0.32). Even, the BDP_{AOD} was 46 % higher

24 compared to decadal average for the station (0.67±0.28; Kumar et al., 2018). Figure 7a also includes a

25 comparison of relative dominance of aerosol types in terms of AE, and in both conditions fine particles

26 (AE; BDP: 1.5, BLDP: 1.7) were found to dominate with a season specific mean (±1σ) of 1.6 (±0.2).

27   Following the evidence of persisting high AOD and high AE indicating dominance of fine

28 particulates of anthropogenic origin, the nature of aerosols in terms of absorbing and/-or scattering

29 was distinguished using OMI UVAI. UVAI has been widely used to detect dust (Badarinath et al., 2010),

30 biomass burning aerosols (Torres et al., 2013; Kaskaoutis et al., 2014) and soot particles (Kumar et al.,

31 2016), and has also been used in combination with CALIPSO to detect height of aerosol layer (Guan et

32 al., 2010). In our experiment, the daily UVAI varied from (-) 0.34 to (+) 2.24 with a seasonal mean (±1σ)

33 of 0.99 (±0.49) over IGP, which is considerably higher than the seasonal mean for entire South Asia

1 (0.47±0.46). Interestingly, negative UVAI was only evident during early October (week 1) signifying
2 presence of non-absorbing aerosols (like sulphate), while UV absorbing aerosols such as smoke and/-
3 or mineral dust was mainly evident during rest of the season. During BDP, the high UVAI values (>1.5)
4 were mainly found to concentrate over the upper to middle IGP with 72 % of observations remain
5 >1.0. This clearly indicates the larger abundance of fresh UV-absorbing particles, and is similar to the
6 reported UVAI (<2.0) over the Himalayas during peak burning season (Kumar et al., 2011; Vadrevu et
7 al., 2012). There was also considerable difference between the periodical mean UVAI for BDP
8 (1.47±0.64) and BLDP (0.75±0.58) over the ground station. Further, following Guan et al. (2010) to use
9 UVAI as a proxy to compute aerosol height, we found a low average height of aerosol layer (~1.5 km),
10 possibly due to low-altitude injection of plumes from burning of agricultural residues.

11   Apart from aerosols, spatial variation of few trace gases (e.g. CO and NO_2), directly emitted
12 from biomass burning are also estimated. The MERRA-2 reanalysis surface CO profile was consistent
13 with the observed UVAI, with high CO surface concentration over IGP (mean±SD: 156±62 ppbv) in
14 contrast to South Asia (114±52 ppbv). Similar was the case for tropospheric NO_2 column density as
15 Aura OMI observation show high NO_2 concentration across IGP (2.4±1.1 x10^{15} mol.cm^{-2}) compared to
16 South Asia (1.5±1.0 x10^{15} mol.cm^{-2}). Dominance of CO and NO_2 across IGP clearly reflect the influence
17 of anthropogenic emissions from industries, vehicles and biomass burning. Likewise, higher surface
18 NO_2 concentrations (> 5x10^{15} mol cm^2) were particularly evident over urban/-industrial hotspots like
19 Punjab and Delhi, over industrial sectors in the Chhattisgarh and in lower IGP (particularly over Dhaka).
20 Temporal variations in mean CO (143 to 169 ppbv) and NO_2 concentrations (2.3 to 2.5 x10^{15} mol cm^{-2})
21 were not so severe both across IGP and over ground station (CO: 140-142 ppbv; NO_2: 2.3-2.5 x10^{15} mol
22 cm^{-2}). The possible explanation for such minimum episode-specific variation may be the short
23 residence time of NO_2 and CO, as NO_2 rapidly photo-dissociate by reaction with OH radical, while CO
24 gradually oxidized to form CO_2. Overall, spatio-temporal nature of aerosols and trace gases were
25 consistent with the observed trend at the ground station and were prudent for establishing the
26 influence of biomass emissions over the region.

27 **3.7 Vertical distribution of aerosols**

28   Vertically resolved aerosol subtypes from spaceborne lidar for selected overpasses across IGP
29 are plotted in Fig. 8a, with corresponding extinction coefficient of aerosol type (Fig. 8b). The CALIPSO-
30 CALIOP profile clearly indicates a temporal change in aerosol type, without any considerable change
31 in the height of aerosol layer. During initial days (in October), dominance of polluted dust (dust mixed
32 with biomass burning smoke) were noted across IGP, with occasional prevalence of smoke (biomass
33 burning aerosols), clean continental (clean background aerosol) and dust aerosols. However, the
34 contribution of polluted dust to total aerosol extinction was higher compared to the rest of aerosol

type. The height of aerosol layer was relatively low (<2 km) corresponding to a low plume injection height and thereby, pose limited potential for dispersion. The aerosol vertical profile however, modified from the end of October due to biomass burning emissions, with dominance of smoke particles, mainly persisting at low altitude (<1.5 km). The height of smoke layer was consistent to that of OMI UVAI projected aerosol height. Smoke particles were found to associate with polluted dust, clean continental and polluted continental, with overlapping profiles. Overall, smoke was the most frequent aerosol type with high aerosol extinction coefficient (1-2.5 Km^{-1} at 532 nm), and the altitude of largest occurrence frequency of smoke remain below ~1.5 km. The low injection height of smoke plumes from biomass burning may serve as a key input for aerosol transport modeling over IGP, as it critically regulates the distance and direction of the particle dispersion (Guan et al., 2010; Banerjee et al., 2011).

The daily variation in total aerosol extinction and aerosol extinction only by smoke particles were also included in Fig. 8c. Total aerosol extinction indicates a corresponding increase during biomass burning which peaks particularly in November, with low smoke injection height. Clear evidence of gradual increase in smoke particle aerosol extinction was also noted. A single evidence of high smoke extinction (>1 Km^{-1}) at a greater height (~ 3.4 km) was noted on November 11, which may be associated to particle long-range transport and/-or by the influence of ABL. Overall, the CALIOP aerosol profiles were in accordance to the ground observations and OMI UVAI, referring exclusive dominance of high UV-absorbing aerosols across the plain during intense biomass burning.

3.8 Potential aerosols sources and transport

Active fire counts from the Terra and Aqua MODIS fires and thermal anomalies (with ≥70% confidence) clearly indicate that fire spots were predominately over the upper IGP, mainly concentrated over the Indian state of Punjab, Haryana and western Uttar Pradesh, and in Punjab state of Pakistan (Fig. 9). However, there was a temporal shift in the total number of fire counts (Fig. 9, within the marked region) from biomass burning dominating period (BDP: 5272) to a less dominating period (BLDP: 4466). Even, the Fire Radiative Power (FRP) i.e. rate of energy released in unit time indicates a relative change in amount and strength of biomass burning emissions, mainly during BDP (138,366 MW) in comparison to BLDP (112,168 MW). The total FRP was higher during BDP mainly due to higher number of fire counts and fire strength, as the rate of release of thermal radiation is related to the amount of biomass burnt and smoke being released (Schroeder et al., 2010). The MODIS fire spots (with brightness temperature), specially subset over IGP were plotted against five days air-mass back trajectories, simulated and integrated at three vertical heights (100m, 300m and 500m) over the ground station. Vertical heights were selected based on the average planetary boundary layer height (402±81 m) for the monitoring period. The air-mass back trajectories indicate the upper IGP as the

1   sole source of aerosols during BDP, which was otherwise influenced by both continental and marine

2   air-masses during non-dominating period. The air-mass back trajectories during BDP overlap precisely

3   on the fire spots that corresponds to higher brightness temperature, referring greater relevance to

4   FRP. The air masses for individual episode were further subject to cluster and CWT analysis considering

5   columnar aerosol load, and result was consistent with our prior observations. High CWT (>0.8) during

6   BDP was clearly attributed to the regional pollution, mainly originated from the upper IGP. In contrast,

7   relatively low CWT was noted during BLDP, originating both from upper IGP (CWT<0.8), western dry

8   region (CWT<0.6) and few from oceanic environment (CWT<0.4). This leads us to conclude with

9   confidence that there was a strong temporal gradient in post-monsoon specific biomass burning

10   emission over the upper IGP, which greatly influence the regional aerosol climatology and thereby,

11   influence the aerosol-induced health effects and regional climate.

12   **3.9 Aerosol radiative forcing and atmospheric heating**

13   Daily satellite retrieved AOD, TCO, CWV, SSA, ground-based BC mass concentration, aerosol

14   water soluble and insoluble fractions were used as an input to OPAC model to simulate aerosol

15   radiative forcing (ARF at 0.2-4.0 μm). Within the period, TCO varied between 237 to 277 DU without

16   any difference between BDP (257±10 DU) and BLDP (256±12 DU). The SSA (at 550nm), designates the

17   fraction of scattered light over the total light extinction, was lower during BDP (0.86±0.05) compared

18   to BLDP (0.98±0.04), suggesting abundance of strong absorbing aerosols especially during BDP. The

19   CWV also fluctuates considerably (range: 0.28-3.92 cm) with overall season specific mean (±σ) of 2.0

20   (±0.7) cm.

21   The direct ARF and heating rate were estimated under clear-sky conditions with SBDART

22   model using OPAC output. The composite ARF was calculated for individual episodes at surface (SRF),

23   top of the atmosphere (TOA) and atmosphere (ATM) (Fig. 10). Overall, the ARF at TOA and SRF were

24   negative, indicating the aerosol cooling effect at surface and at top-of-the-atmosphere. There was a

25   slight temporal change in TOA radiative forcing (BDP: -28; BLDP: -23 W m^{-2}) compared to the

26   considerable intra-seasonal variation in SRF forcing (BDP: -163; BLDP: -79 W m^{-2}). The variation in SRF

27   forcing was mainly induced by the surface BC (mean; BDP, BLDP: 9, 7 μg m^{-3}), aerosol mass

28   concentration (501, 327 μg m^{-3}) and WSIC fractions, particularly in SO_4^{2-} (38, 15 μg m^{-3}), NO_3^- (19, 12

29   μg m^{-3}) and NH_4^+ (11, 4 μg m^{-3}). Since the ATM forcing is the balance of attenuation of radiation at TOA

30   and SRF, the resultant atmospheric forcing was found very high, especially during biomass burning

31   dominated period (BDP: 135 W m^{-2}), compared to non-dominating one (BLDP: 56 Wm^{-2}). Overall, there

32   was a clear indication of intraseasonal variation in aerosol radiative forcing, which needs to consider

33   in parametrization of aerosol schemes for regional climate model. Similarly, the corresponding heat

34   rate was substantially high during BDP (4.3 K day^{-1}), possibly influenced by more absorbing aerosols,

compared to BLDP (1.8 K day^{-1}). The computed ARF during post-monsoon was comparable to other urban sites in Indo-Gangetic Plain that are reported to be influenced by biomass burning e.g. Delhi (44-131 W m^{-2}, Bisht et al., 2015), Patiala (57-63 W m^{-2}, Sharma et al. 2017), Kanpur (30-43 W m^{-2}, Kaskaoutis et al., 2013) and over Karachi (35-84 W m^{-2}, Alam et al., 2011). However, none of the earlier reports noted the intraseasonality in ARF by means of change in driving factors which, appeared to be significant, and necessitate proper addressing in regional model simulation. Intraseasonality in ARF was earlier reported over Varanasi during winter (ARF: 31-47 W m^{-2}, Kumar et al., 2017b), while the change in forcing was not as drastic as evident during post-monsoon. Therefore, it is extremely likely that intraseasonality in aerosol properties significantly influence the aerosol-climate-health interactions over IGP and therefore, must need to be taken in to account for uncertainty analysis in the regional aerosol/-climate model.

4. Conclusions

The influence of biomass burning emissions on aerosol properties, transport and radiative forcing was evaluated over Indo-Gangetic plain, South Asia. Very high concentration of total and fine mode aerosol (PM$_{2.1}$) were observed during post-monsoon, with significant increase in fine to coarse particle ratio (>1) particularly from November. Submicron particles dominate the aerosol fine mode, with PM$_{1.1}$ to PM$_{1.1-2.1}$ ratio frequently exceeding 2.5. The WSIS was found to constitute greater proportion of submicron and fine particle mass compared to the coarser one. The WSIS was mainly of secondary nature, with major contribution from sulfate and nitrate ions. A strong correlation between NH$_4^+$ and SO$_4^{2-}$, and high NH$_4^+$/SO$_4^{2-}$ equivalent ratio in submicron particulates indicate the abundance of gaseous NH$_3$ to neutralize acidic species (SO$_4^{2-}$). This contrasted with coarse mode particles where low NH$_4^+$/SO$_4^{2-}$ equivalent ratio refers the predominant neutralization by crustal minerals. The NO$_3^-$ to SO$_4^{2-}$ ratio for submicron and fine mode particles also increased (>1) during extreme biomass emissions, as expected considering other reported observations of haze events over Asia. A rise in black carbon with corresponding increase in Delta-C refer to the added contribution of biomass burning emissions. The influence of emissions was further quantified using specific organic (Levoglucosan), inorganic (K$^+$ and NH$_4^+$) and satellite (UVAI) tracers. Levoglucosan was the most abundant species in submicron particles, with a very high ratio (>50) against other anhydrosugars denoting exclusive emissions from burning of agriculture residues. The temporal variation in levoglucosan was consistent with inorganic tracers (K$^+$ and NH$_4^+$), with a sharp rise during November, and a strong correlation between these three indicates their biogenic sources. The association between levoglucosan and K$^+$ or NH$_4^+$ was non-linear, with an exponential fit for submicron and fine particulates. The spatio-temporal distribution of aerosols was evaluated in terms of area weighted mean both over IGP and over the selected transect across ground station. During biomass burning

dominated period, a considerable increase in columnar aerosol loading was highlighted (AOD: 0.98), consisting absorbing aerosols (UVAI > 1.5) with a corresponding low plume height (~1.5 km). Moreover, the variation of few trace gases associated with biomass emissions (CO and NO_2) were consistent with AOD, allowing a definite spatial signature of emissions sources and transport across IGP. The CALIPSO-CALIOP cross-sectional altitudinal profiles clearly illustrate the intraseasonality in aerosol types that were dominated by smoke and polluted continental aerosols during biomass emissions, which otherwise associate to clean continental, polluted dust and dust aerosols. The possible pathway for regional transport of aerosols from upper IGP to the ground station was noted using cluster analysis and concentration weighted air mass back-trajectories. Finally, aerosol optical and micro-physical properties were used in combination to simulate direct aerosol radiative forcing (ARF) and atmospheric heating. There was evidence of strong intraseasonality in ARF with very high atmospheric forcing (135 Wm^{-2}) and heating rate (4.3 $Kday^{-1}$) during biomass burning dominated period compared to non-dominating one (56 Wm^{-2}, 1.8 $Kday^{-1}$).

Considering that the duration of these biomass burning emissions represents several weeks per year, there impact on ARF and by consequent on the regional climate is not negligible. We therefore, conclude with reasonable level of confidence that intraseasonality in aerosol properties must be seriously considered in the regional aerosol-climate model, for improve assessment and forecasting of aerosol-climate-health interactions across IGP.

Data availability

MODIS data are available at Level 1 Atmosphere Archive & Distribution System (LAADS) at https://ladsweb.nascom.nasa.gov. Aura-OMI and MERRA 2 reanalysis data are available at Mirador-NASA Goddard Earth Sciences Data and Information Center (GES DISC) (https://mirador.gsfc.nasa.gov). CALIPSO data are available at NASA Atmospheric Science Data Center (https://eosweb.larc.nasa.gov). Planetary Boundary Layer height and air mass back-trajectories are retrieved from Global Data Assimilation System (GDAS) archives hosted at NOAA-Air Resource Laboratory (https://ready.arl.noaa.gov). Modis Fire products are obtained from Fire Information for Resource Management System (FIRMS) (https://firms.modaps.eosdis.nasa.gov). Trace gases data at ground station are available at Real time Air Quality Data inventory of Central Pollution Control Board (https://app.cpcbccr.com/ccr).

Team List. Nandita Singh (NS), Tirthankar Banerjee (TB), Made P. Raju (MPR), Karine Deboudt (KD), Meytar Sorek-Hamer (MSH), Ram S. Singh (RSS) and Rajesh K. Mall (RKM).

Author Contributions

N.S. and T.B. designed the experiment while N.S., M.P.R. and T.B. carried out the experiment and analyzed the data. N.S., M.P.R., K.D., T.B., R.S.S., R.K.M. and M.S.H. interpreted the observation and N.S., T.B. and K.D. drafted the manuscript.

Competing interests. The authors declare that they have no conflict of interest.

Acknowledgements

References

Alam, K., Trautmann, T., and Blaschke, T.: Aerosol optical properties and radiative forcing over mega-city Karachi, Atmos. Res., 101, 773-782, https://doi.org/10.1016/j.atmosres.2011.05.007, 2011.

Apte, J.S., Marshall, J.D., Cohen, A.J., and Brauer, M.: Addressing global mortality from ambient PM2. 5, Environ. Sci. Technol., 49, 8057-8066, https://pubs.acs.org/doi/10.1021/acs.est.5b01236, 2015.

Badarinath, K.V.S., Sharma, A.R., Kaskaoutis, D.G., Kharol, S.K., and Kambezidis, H.D.: Solar dimming over the tropical urban region of Hyderabad, India: Effect of increased cloudiness and increased anthropogenic aerosols. J. Geophys. Res.-Atmos., 115, D21208, https://doi.org/10.1029/2009JD013694, 2010.

Banerjee, T., Murari, V., Kumar, M., and Raju, M.P.: Source apportionment of airborne particulates through receptor modeling: Indian scenario. Atmos. Res., 164, 167-187, https://doi.org/10.1016/j.atmosres.2015.04.017, 2015.

Banerjee, T., Barman, S.C., Srivastava, R.K.: Application of air pollution dispersion modeling for source-contribution assessment and model performance evaluation at Integrated Industrial Estate-Pantnagar. Environ Pol., 159, 865-875, https://doi.org/10.1016/j.envpol.2010.12.026, 2011.

Bellouin, N., Boucher, O., Haywood, J., and Reddy, M.S.: Global estimate of aerosol direct radiative forcing from satellite measurements, Nature, 438, 1138–1141, https://doi.org/10.1038/nature04348, 2005.

Bisht, D.S., Dumka, U.C., Kaskaoutis, D.G., Pipal, A.S., Srivastava, A.K., Soni, V.K., Attri, S.D., Sateesh, M., and Tiwari, S.: Carbonaceous aerosols and pollutants over Delhi urban environment: temporal evolution, source apportionment and radiative forcing, Sci. Total Environ., 521, 431-445, https://doi.org/10.1016/j.scitotenv.2015.03.083, 2015.

Bodhaine, B.A.: Aerosol absorption measurements at Barrow, Mauna Loa and the south pole, J. Geophys. Res.-Atmos., 100, 8967-8975, https://doi.org/10.1029/95JD00513, 1995.

Bond, T.C., Doherty, S.J., Fahey, D.W., Forster, P.M., Berntsen, T., DeAngelo, B.J., Flanner, M.G., Ghan, S., Kärcher, B., Koch, D., and Kinne, S.: Bounding the role of black carbon in the climate system: A scientific assessment, J. Geophys. Res.-Atmos., 118, 5380-5552, https://doi.org/10.1002/jgrd.50171, 2013.

Chang-Graham, A.L., Profeta, L.T., Johnson, T.J., Yokelson, R.J., Laskin, A. and Laskin, J.: Case study of water-soluble metal containing organic constituents of biomass burning aerosol, Environ. Sci. Technol., 45,1257-1263, https://doi.org/10.1021/es103010j, 2011.

Cheng, Y., Engling, G., He, K.B., Duan, F.K., Ma, Y.L., Du, Z.Y., Liu, J.M., Zheng, M., and Weber, R.J.: Biomass burning contribution to Beijing aerosol, Atmos. Chem. Phys., 13(15), 7765-7781, https://doi.org/10.5194/acp-13-7765-2013, 2013.

Chen, P., Kang, S., Li, C., Rupakheti, M., Yan, F., Li, Q., Ji, Z., Zhang, Q., Luo, W., and Sillanpää, M.: Characteristics and sources of polycyclic aromatic hydrocarbons in atmospheric aerosols in the Kathmandu Valley, Nepal, Sci. Total Environ. 538, 86-92, https://doi.org/10.1016/j.scitotenv.2015.08.006, 2015.

Draxler, R.R., and Rolph, G.D., 2003. HYSPLIT (HYbrid single-particle Lagrangian integrated trajectory) model access via NOAA ARL READY. NOAA Air Resources Laboratory, Silver Spring, MD. Dostupno na: http://ready. arl. noaa. gov/HYSPLIT. php (06. 06. 2010.).

Engling, G., Lee, J.J., Tsai, Y.W., Lung, S.C.C., Chou, C.C.K., and Chan, C.Y.: Size-resolved anhydrosugar composition in smoke aerosol from controlled field burning of rice straw, Aerosol Sci. Technol., 43, 662-672, https://doi.org/10.1080/02786820902825113, 2009.

Fu, P., Kawamura, K., Okuzawa, K., Aggarwal, S.G., Wang, G., Kanaya, Y., and Wang, Z.: Organic molecular compositions and temporal variations of summertime mountain aerosols over Mt. Tai, North China Plain, J. Geophys. Res.-Atmos., 113, D19107, https://doi.org/10.1029/2008JD009900, 2008.

Gonzalez, R.O., Strekopytov, S., Amato, F., Querol, X., Reche, C., and Weiss, D.: New insights from zinc and copper isotopic compositions into the sources of atmospheric particulate matter from two major European cities, Environ. Sci. Technol., 50, 9816-9824, https://pubs.acs.org/doi/10.1021/acs.est.6b00863, 2016.

Guan, H., Esswein, R., Lopez, J., Bergstrom, R., Warnock, A., Follette-Cook, M., Fromm, M., and Iraci, L.T.: A multi-decadal history of biomass burning plume heights identified using aerosol index measurements, Atmos. Chem. Phys., 10, 6461-6469, https://doi.org/10.5194/acp-10-6461-2010, 2010.

Hess, M., Koepke, P., and Schult, I.: Optical properties of aerosols and clouds: The software package OPAC, Bull. Am. Meteorol. Soc., 79, 831-844, https://doi.org/10.1175/1520-0477(1998)079<0831:OPOAAC>2.0.CO;2, 1998.

Hu, Q.H., Xie, Z.Q., Wang, X.M., Kang, H., and Zhang, P.: Levoglucosan indicates high levels of biomass burning aerosols over oceans from the Arctic to Antarctic, Sci. Rep., 3, 3119, https://doi.org/10.1038/srep03119, 2013.

Jimenez, J.L., Canagaratna, M.R., Donahue, N.M., Prevot, A.S.H., Zhang, Q., Kroll, J.H., DeCarlo, P.F., Allan, J.D., Coe, H., Ng, N.L., and Aiken, A.C.: Evolution of organic aerosols in the atmosphere, Science, 326, 1525-1529, http://doi.org/10.1126/science.1180353, 2009.

Justice, C., Giglio, L., Boschetti, L., Roy, D., Csiszar, I., Morisette, J., and Kaufman, Y.: MODIS Fire Products Algorithm Technical Background Document. MODIS Science Team, 2006.

Kanakidou, M., Myriokefalitakis, S., and Tsigaridis, K.: Aerosols in atmospheric chemistry and biogeochemical cycles of nutrients. Environ. Res. Lett., in press, https://doi.org/10.1088/1748-9326/aabcdb, 2018.

Kaskaoutis, D.G., Kumar, S., Sharma, D., Singh, R.P., Kharol, S.K., Sharma, M., Singh, A.K., Singh, S., Singh, A., and Singh, D.: Effects of crop residue burning on aerosol properties, plume characteristics, and long-range transport over northern India, J. Geophys. Res.-Atmos., 119, 5424-5444, https://doi.org/10.1002/2013JD021357, 2014.

Kaskaoutis, D.G., Sinha, P.R., Vinoj, V., Kosmopoulos, P.G., Tripathi, S.N., Misra, A., Sharma, M., and Singh, R.P.: Aerosol properties and radiative forcing over Kanpur during severe aerosol loading conditions, Atmos. Environ., 79, 7-19, https://doi.org/10.1016/j.atmosenv.2013.06.020, 2013.

Krotkov, N.A., Lamsal, L.N., Celarier, E.A., Swartz, W.H., Marchenko, S.V., Bucsela, E.J., Chan, K.L., Wenig, M., and Zara, M.: The version 3 OMI NO 2 standard product, Atmospheric Meas. Tech., 10, 3133-3149, https://doi.org/10.5194/amt-10-3133-2017, 2017.

Kumar, M., Tiwari, S., Murari, V., Singh, A.K., and Banerjee, T.: Wintertime characteristics of aerosols at middle Indo-Gangetic Plain: Impacts of regional meteorology and longrange transport, Atmos. Environ., 104, 162-175, https://doi.org/10.1016/j.atmosenv.2015.01.014, 2015a.

Kumar, R., M.C. Barth, G.G. Pfister, V.S. Nair, S.D. Ghude, and N. Ojha.: What controls the seasonal cycle of black carbon aerosols in India?, J. Geophys. Res. Atmos., 120, 7788–7812, doi:10.1002/2015JD023298, 2015b.

Kumar, M., Parmar, K.S., Kumar, D.B., Mhawish, A., Broday, D.M., Mall, R.K., and Banerjee, T.: Long-term aerosol climatology over Indo-Gangetic Plain: Trend, prediction and potential source fields, Atmos. Environ., 180, 37-50, https://doi.org/10.1016/j.atmosenv.2018.02.027, 2018.

Kumar, M., Raju, M.P., Singh, R.S., and Banerjee, T.: Impact of drought and normal monsoon scenarios on aerosol induced radiative forcing and atmospheric heating in Varanasi over middle Indo-Gangetic Plain, J. Aerosol Sci., 113, 95-107, https://doi.org/10.1016/j.jaerosci.2017.07.016, 2017a.

Kumar, M., Raju, M.P., Singh, R.K., Singh, A.K., Singh, R.S., and Banerjee, T.: Wintertime characteristics of aerosols over middle Indo-Gangetic Plain: Vertical profile, transport and radiative forcing, Atmos. Res., 183, 268-282, https://doi.org/10.1016/j.atmosres.2016.09.012, 2017b.

Kumar, M., Singh, R.K., Murari, V., Singh, A.K., Singh, R.S., and Banerjee, T.: Fireworks induced particle pollution: a spatio-temporal analysis, Atmos. Res., 180, 78-91, https://doi.org/10.1016/j.atmosres.2016.05.014, 2016.

Kumar, R., Naja, M., Satheesh, S.K., Ojha, N., Joshi, H., Sarangi, T., Pant, P., Dumka, U.C., Hegde, P., and Venkataramani, S.: Influences of the springtime northern Indian biomass burning over the central Himalayas, J. Geophys. Res.-Atmos., 116, D19302, https://doi.org/10.1029/2010JD015509, 2011.

Kang, M., Fu, P., Aggarwal, S.G., Kumar, S., Zhao, Y., Sun, Y., and Wang, Z.: Size distributions of n-alkanes, fatty acids and fatty alcohols in springtime aerosols from New Delhi, India, Environ. Pollut., 219, 957-966, https://doi.org/10.1016/j.envpol.2016.09.077, 2016.

Levelt, P.F., van den Oord, G.H., Dobber, M.R., Malkki, A., Visser, H., de Vries, J., Stammes, P., Lundell, J.O., and Saari, H.: The ozone monitoring instrument, IEEE Trans. Geosci. Remote Sens., 44, 1093-1101, http://doi.org/10.1109/TGRS.2006.872333, 2006.

Levy, R.C., Mattoo, S., Munchak, L.A., Remer, L.A., Sayer, A.M., Patadia, F., and Hsu, N.C.: The Collection 6 MODIS aerosol products over land and ocean, Atmospheric Meas. Tech., 6, 2989-3034, https://doi.org/10.5194/amt-6-2989-2013, 2013.

Li, J., Wang, G., Aggarwal, S.G., Huang, Y., Ren, Y., Zhou, B., Singh, K., Gupta, P.K., Cao, J., and Zhang, R.: Comparison of abundances, compositions and sources of elements, inorganic ions and organic compounds in atmospheric aerosols from Xi'an and New Delhi, two megacities in China and India, Sci. Total Environ., 476, 485-495, https://doi.org/10.1016/j.scitotenv.2014.01.011, 2014.

Mochida, M., Umemoto, N., Kawamura, K., Lim, H.J., and Turpin, B.J.: Bimodal size distributions of various organic acids and fatty acids in the marine atmosphere: Influence of anthropogenic aerosols, Asian dusts, and sea spray off the coast of East Asia, J. Geophys. Res.-Atmos., 112, D15209, https://doi.org/10.1029/2006JD007773, 2007.

Mhawish, A., Banerjee, T., Broday, D.M., Misra, A., and Tripathi, S.N.: Evaluation of MODIS Collection 6 aerosol retrieval algorithms over Indo-Gangetic Plain: Implications of aerosols types and mass loading, Remote Sens. Environ., 201, 297-313, https://doi.org/10.1016/j.rse.2017.09.016, 2017.

Mhawish, A., Kumar, M., Mishra, A.K., Srivastava, P.K., and Banerjee, T.: Remote sensing of aerosols from space: retrieval of properties and applications, In Remote Sensing of Aerosols, Clouds, and Precipitation, 45-83, https://doi.org/10.1016/B978-0-12-810437-8.00003-7, 2018.

Moorthy, K.K., Satheesh, S.K., Babu, S.S., and Dutt, C.B.S.: Integrated Campaign for Aerosols, gases and Radiation Budget (ICARB): An overview, J. Earth Syst. Sci., 117, 243–262, https://doi.org/10.1007/s12040-008-0029-7, 2008.

Murari, V., Kumar, M., Barman, S.C., and Banerjee, T.: Temporal variability of MODIS aerosol optical depth and chemical characterization of airborne particulates in Varanasi, India, Environ. Sci. Pollut. Res., 22, 1329-1343, https://doi.org/10.1007/s11356-014-3418-2, 2015.

Murari, V., Kumar, M., Mhawish, A., Barman, S.C., and Banerjee, T.: Airborne particulate in Varanasi over middle Indo-Gangetic Plain: variation in particulate types and meteorological influences, Environ. Monit. Assess., 189, 157, https://doi.org/10.1007/s10661-017-5859-9, 2017.

Murari, V., Kumar, M., Singh, N., Singh, R.S., and Banerjee, T.: Particulate morphology and elemental characteristics: variability at middle Indo-Gangetic Plain, J. Atmos. Chem., 73, 165-179, https://doi.org/10.1007/s10874-015-9321-5, 2016.

Myhre, G., Samset, B.H., Schulz, M., Balkanski, Y., Bauer, S., Berntsen, T.K., Bian, H., Bellouin, N., Chin, M., Diehl, T., and Easter, R.C.: Radiative forcing of the direct aerosol effect from AeroCom Phase II simulations, Atmos. Chem. Phys., 13, 1853-1877, https://doi.org/10.5194/acp-13-1853-2013, 2013.

Pavuluri, C.M., Kawamura, K., Aggarwal, S.G., and Swaminathan, T.: Characteristics, seasonality and sources of carbonaceous and ionic components in the tropical aerosols from Indian region, Atmos. Chem. Phys., 11, 8215-8230, https://doi.org/10.5194/acp-11-8215-2011, 2011.

Prajapati, S.K., and Tripathi, B.D.: Seasonal variation of leaf dust accumulation and pigment content in plant species exposed to urban particulates pollution, J. Environ. Qual., 37, 865-870, https://doi.org/10.2134/jeq2006.0511, 2008.

Rajput, P., and Sarin, M.M.: Polar and non-polar organic aerosols from large-scale agricultural-waste burning emissions in Northern India: implications to organic mass-to-organic carbon ratio, Chemosphere, 103, 74-79, https://doi.org/10.1016/j.chemosphere.2013.11.028, 2014.

Rajput, P., Sarin, M. M., Sharma, D., and Singh, D.: Characteristics and emission budget of carbonaceous species from post-harvest agricultural-waste burning in source region of the Indo-Gangetic Plain, Tellus B, 66, 21026, https://doi.org/10.3402/tellusb.v66.21026, 2014

Rajput, P., Sarin, M.M., Rengarajan, R., and Singh, D.: Atmospheric polycyclic aromatic hydrocarbons (PAHs) from post-harvest biomass burning emissions in the Indo-Gangetic Plain: isomer ratios and temporal trends, Atmos. Environ., 45, 6732-6740, https://doi.org/10.1016/j.atmosenv.2011.08.018, 2011.

Raju, M.P., Safai, P.D., Vijayakumar, K., Devara, P.C.S., Naidu, C.V., Rao, P.S.P., and Pandithurai, G.: Atmospheric abundances of black carbon aerosols and their radiative impact over an urban and a rural site in SW India, Atmos. Environ., 125, 429-436, https://doi.org/10.1016/j.atmosenv.2015.09.023, 2016.

Ricchiazzi, P., Yang, S., Gautier, C., and Sowle, D.: SBDART: A research and teaching software tool for plane-parallel radiative transfer in the Earth's atmosphere, Bull. Am. Meteorol. Soc., 79, 2101-2114, https://doi.org/10.1175/1520-0477(1998)079<2101:SARATS>2.0.CO;2, 1998.

Riipinen, I., Pierce, J.R., Yli-Juuti, T., Nieminen, T., Hakkinen, S., Ehn, M., Junninen, H., Lehtipalo, K., Petaja, T., Slowik, J., and Chang, R.: Organic condensation: a vital link connecting aerosol formation to cloud condensation nuclei (CCN) concentrations, Atmos. Chem. Phys., 11, 3865-3878, https://doi.org/10.5194/acp-11-3865-2011, 2011.

Rogers, R.R., Hostetler, C.A., Hair, J.W., Ferrare, R.A., Liu, Z., Obland, M.D., Harper, D.B., Cook, A.L., Powell, K.A., Vaughan, M.A., and Winker, D.M.: Assessment of the CALIPSO Lidar 532 nm attenuated backscatter calibration using the NASA LaRC airborne High Spectral Resolution Lidar, Atmos. Chem. Phys., 11, 1295-1311, https://doi.org/10.5194/acp-11-1295-2011, 2011.

Ryu, S.Y., Kim, J.E., Zhuanshi, H., Kim, Y.J. and Kang, G.U.: Chemical composition of post-harvest biomass burning aerosols in Gwangju, Korea, J. Air Waste Manag. Assoc., 54, 1124-1137, https://doi.org/10.1080/10473289.2004.10471018, 2004.

Sayer, A.M., Munchak, L.A., Hsu, N.C., Levy, R.C., Bettenhausen, C., and Jeong, M.J.: MODIS Collection 6 aerosol products: Comparison between Aqua's e-Deep Blue, Dark Target, and "merged" data sets, and usage recommendations, J. Geophys. Res.-Atmos., 119, 13,965–13,989, https://doi.org/10.1002/2014JD022453, 2014.

Schkolnik, G., Falkovich, A.H., Rudich, Y., Maenhaut, W., and Artaxo, P.: New analytical method for the determination of levoglucosan, polyhydroxy compounds, and 2-methylerythritol and its application to smoke and rainwater samples, Environ. Sci. Technol., 39, 2744-2752, http://doi.org/10.1021/es048363c, 2005.

Schroeder, W., Csiszar, I., Giglio, L., and Schmidt, C.C.: On the use of fire radiative power, area, and temperature estimates to characterize biomass burning via moderate to coarse spatial resolution remote sensing data in the Brazilian Amazon, J. Geophys. Res.-Atmos., 115, D21121, https://doi.org/10.1029/2009JD013769, 2010.

Seinfeld, J.H., Bretherton, C., Carslaw, K.S., Coe, H., DeMott, P.J., Dunlea, E.J., Feingold, G., Ghan, S., Guenther, A.B., Kahn, R., and Kraucunas, I.: Improving our fundamental understanding of the role of aerosol– cloud interactions in the climate system, Proc. Natl. Acad. Sci., 113, 5781-5790, https://doi.org/10.1073/pnas.1514043113, 2016.

Sen, A., Abdelmaksoud, A.S., Ahammed, Y.N., Banerjee, T., Bhat, M.A., Chatterjee, A., Choudhuri, A.K., Das, T., Dhir, A., Dhyani, P.P., and Gadi, R.: Variations in particulate matter over Indo-Gangetic Plains and Indo-Himalayan Range during four field campaigns in winter monsoon and summer monsoon: role of pollution pathways, Atmos. Environ., 154, 200-224, https://doi.org/10.1016/j.atmosenv.2016.12.054, 2017.

Sharma, D., Srivastava, A.K., Ram, K., Singh, A., and Singh, D.: Temporal variability in aerosol characteristics and its radiative properties over Patiala, northwestern part of India: Impact of agricultural biomass burning emissions, Environ. Pollut., 231, 1030-1041, https://doi.org/10.1016/j.envpol.2017.08.052, 2017.

Simoneit, B.R., Schauer, J.J., Nolte, C.G., Oros, D.R., Elias, V.O., Fraser, M.P., Rogge, W.F., and Cass, G.R.: Levoglucosan, a tracer for cellulose in biomass burning and atmospheric particles, Atmos. Environ., 33, 173-182, https://doi.org/10.1016/S1352-2310(98)00145-9, 1999.

Singh, N., Murari, V., Kumar, M., Barman, S.C., and Banerjee, T.: Fine particulates over South Asia: review and meta-analysis of PM2. 5 source apportionment through receptor model, Environ. Pollut., 223, 121-136, https://doi.org/10.1016/j.envpol.2016.12.071, 2017a.

Singh, N., Mhawish, A., Deboudt, K., Singh, R.S., and Banerjee, T.: Organic aerosols over Indo-Gangetic Plain: Sources, distributions and climatic implications, Atmos. Environ., 157, 59-74, https://doi.org/10.1016/j.atmosenv.2017.03.008, 2017b.

Sun, J., and Ariya, P.A.: Atmospheric organic and bio-aerosols as cloud condensation nuclei (CCN): A review, Atmos. Environ. 40, 795–820, https://doi.org/10.1016/j.atmosenv.2005.05.052, 2006.

Tan, J.H., Duan, J.C., Chen, D.H., Wang, X.H., Guo, S.J., Bi, X.H., Sheng, G.Y., He, K.B., and Fu, J.M.: Chemical characteristics of haze during summer and winter in Guangzhou, Atmos. Res., 94, 238-245, https://doi.org/10.1016/j.atmosres.2009.05.016, 2009.

Tian, M., Wang, H., Chen, Y., Yang, F., Zhang, X., Zou, Q., Zhang, R., Ma, Y., and He, K.: Characteristics of aerosol pollution during heavy haze events in Suzhou, China. Atmos. Chem. Phys., 16, 7357-7371, https://doi.org/10.5194/acp-16-7357-2016, 2016.

Torres, O., Ahn, C., and Chen, Z.: Improvements to the OMI near-UV aerosol algorithm using A-train CALIOP and AIRS observations, Atmospheric Meas. Tech., 6, 3257-3270, https://doi.org/10.5194/amt-6-3257-2013, 2013.

Vadrevu, K.P., Ellicott, E., Giglio, L., Badarinath, K.V.S., Vermote, E., Justice, C., and Lau, W.K.: Vegetation fires in the himalayan region–Aerosol load, black carbon emissions and smoke plume heights, Atmos. Environ., 47, 241-251, https://doi.org/10.1016/j.atmosenv.2011.11.009, 2012.

Vakkari, V., Kerminen, V.M., Beukes, J.P., Tiitta, P., Zyl, P.G., Josipovic, M., Venter, A.D., Jaars, K., Worsnop, D.R., Kulmala, M., and Laakso, L.: Rapid changes in biomass burning aerosols by atmospheric oxidation, Geophys. Res. Lett., 41, 2644-2651, https://doi.org/10.1002/2014GL059396, 2014.

Villalobos, A.M., Amonov, M.O., Shafer, M.M., Devi, J.J., Gupta, T., Tripathi, S.N., Rana, K.S., Mckenzie, M., Bergin, M.H. and Schauer, J.J: Source apportionment of carbonaceous fine particulate matter (PM2.5) in two contrasting cities across the Indo-Gangetic plain, Atmos. Pollut. Res., 6, 398-405, https://doi.org/10.5094/APR.2015.044, 2015.

Wan, X., Kang, S., Li, Q., Rupakheti, D., Zhang, Q., Guo, J., Chen, P., Tripathee, L., Rupakheti, M., Panday, A.K., and Wang, W.: Organic molecular tracers in the atmospheric aerosols from Lumbini, Nepal, in the northern Indo-Gangetic Plain: influence of biomass burning, Atmos. Chem. Phys., 17, 8867-8885, https://doi.org/10.5194/acp-17-8867-2017, 2017.

Wang, Y., Hopke, P.K., Rattigan, O.V., Xia, X., Chalupa, D.C., and Utell, M.J.: Characterization of residential wood combustion particles using the two-wavelength aethalometer, Environ. Sci. Technol., 45, 7387-7393, http://doi.org/10.1021/es2013984, 2011.

Wang, Y.Q., Zhang, X.Y., and Arimoto, R.: The contribution from distant dust sources to the atmospheric particulate matter loadings at XiAn, China during spring, Sci. Total Environ., 368, 875-883, https://doi.org/10.1016/j.scitotenv.2006.03.040, 2006.

Wang, R., Balkanski, Y., Boucher, O., Bopp, L., Chappell, A., Ciais, P., Hauglustaine, D., Peñuelas, J. and Tao, S.: Sources, transport and deposition of iron in the global atmosphere, Atmos. Chem. Phys., 15, 6247-6270, https://doi.org/10.5194/acp-15-6247-2015, 2015.

Zdrahal, Z., Oliveira, J., Vermeylen, R., Claeys, M., and Maenhaut, W.: Improved method for quantifying levoglucosan and related monosaccharide anhydrides in atmospheric aerosols and application to samples from urban and tropical locations, Environ. Sci. Technol., 36, 747-753, http://doi.org/10.1021/es015619v, 2002.

Zhang, W., Tong, Y., Wang, H., Chen, L., Ou, L., Wang, X., Liu, G. and Zhu, Y.: Emission of metals from pelletized and uncompressed biomass fuels combustion in rural household stoves in China, Sci. Rep., 4, 5611, https://doi.org/10.1038/srep05611, 2014.

List of figures:

Fig. 1. Geographical location of aerosol ground monitoring station (a), and MODIS aerosol optical depth with NCEP/NCAR composite means of wind vector during monitoring period (b).

Fig. 2. Time series of (a) size segregated particulate mass concentration, (b) particle ratio and (c) daily means of meteorological variables.

Fig. 3. Variation of (a) ions and (b) trace metals in different aerosol size fractions.

Fig. 4. Variation of BC, Delta C and ABL during entire monitoring period.

Fig. 5. Size-segregated particulate bound (a) organic aerosols, and difference in the molecular compositions of (b) *n*-alkanes and (b) fatty acids.

Fig. 6. Temporal variation of trace gases and biomass burning signature molecules (NH_4^+, K^+, Levoglucosan), and their associations within different aerosol size fractions.

Fig. 7. Episode specific spatial distribution of AOD, AE, UVAI, surface CO (ppbv) and tropospheric NO_2 (molecules cm^{-2}) over (a) South Asia and (b) at ground station.

Fig. 8. Aerosol vertical profiles from selected CALIPSO overpasses across ground station (a) aerosol subtypes, (b) extinction coefficients of each aerosol type and (c) time series of extinction profile for total and smoke aerosols.

Fig. 9. Episode specific MODIS fire count, fire radiative power (FRP, MW), brightness temperature (B. Temp., K), and five days air mass back-trajectory along with CWT.

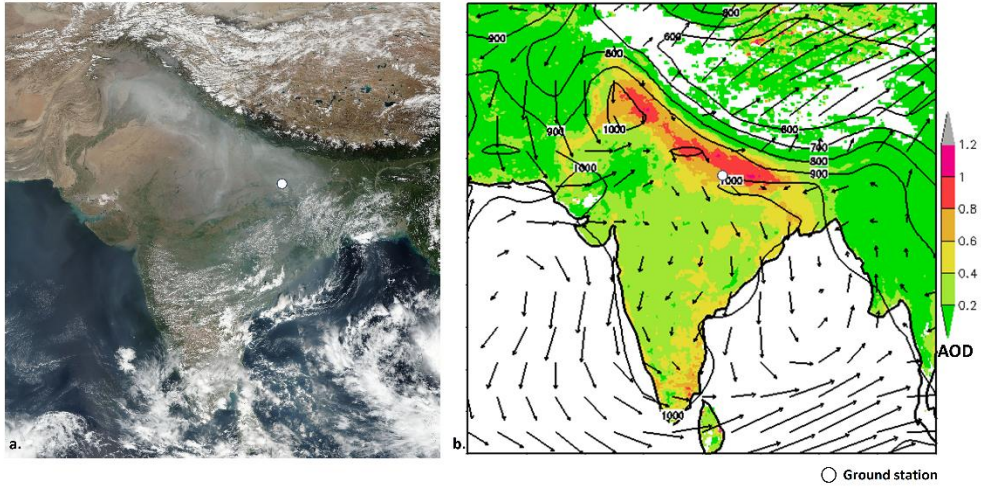Fig. 10. Episode specific aerosol short wave radiative forcing and atmospheric heating.

1

2

3
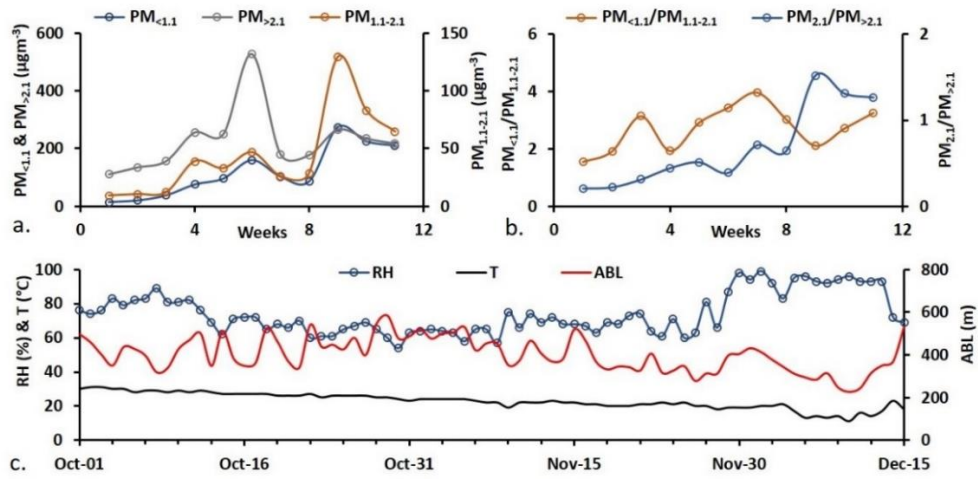

4

5

6 Fig. 1. Geographical location of aerosol ground monitoring station (a), and MODIS aerosol optical
7 depth with NCEP/NCAR composite means of wind vector during monitoring period (b).

8 **Note**: Background image in (a) was retrieved from Suomi NPP VIIRS satellite indicating the thick
9 aerosol layer over north India on October 31, 2016.

10

1

Fig. 2. Time series of (a) size segregated particulate mass concentration, (b) particle ratio and (c) daily means of meteorological variables.

Note: Week 1 to 5 are in the month of October, week 6 to 9 are in November and week 10 to 11 are in December.
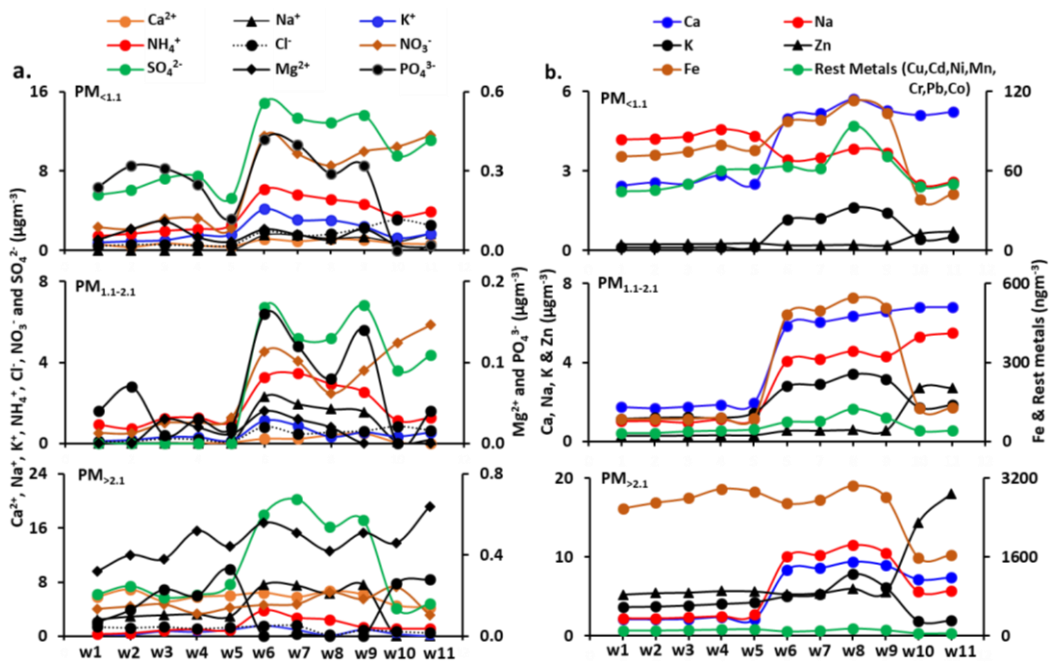
1

Fig. 3. Variation of (a) ions and (b) trace metals in different aerosol size fractions.

Note: Week 1 to 5 are in the month of October, week 6 to 9 are in November and week 10 to 11 are in December.
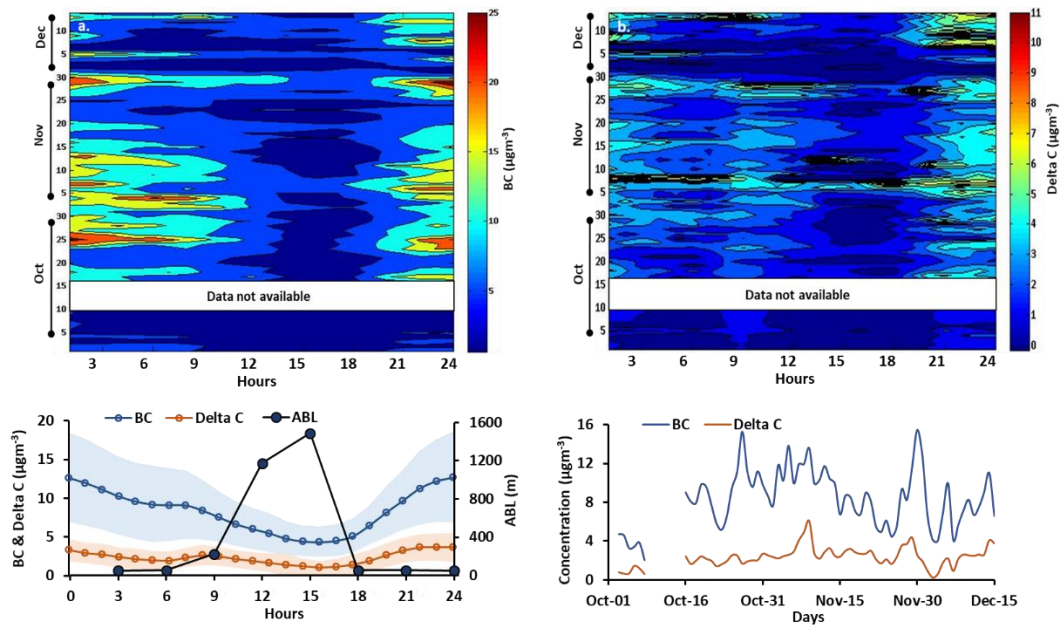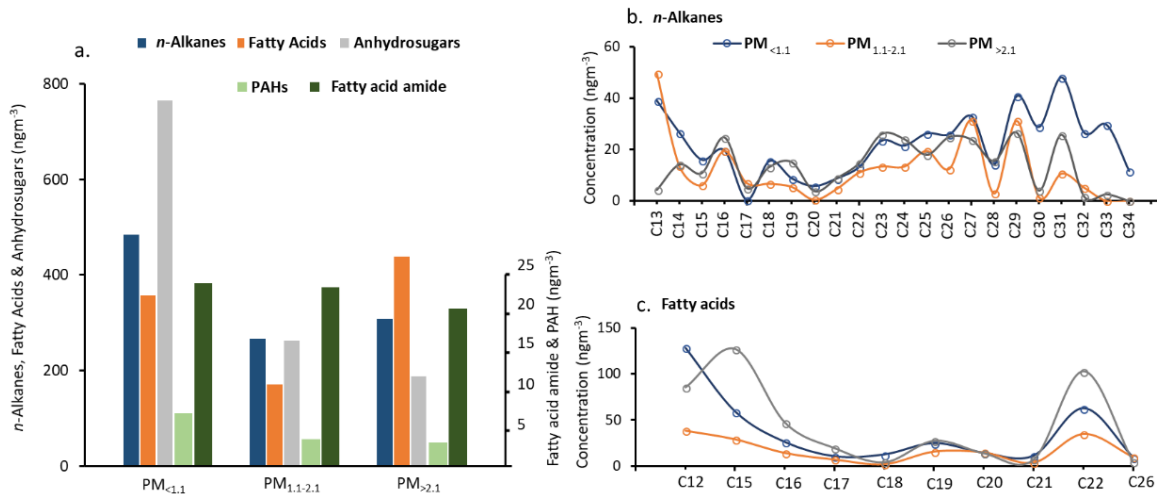
1

2

Fig. 4. Variation of BC, Delta C and ABL during entire monitoring period.

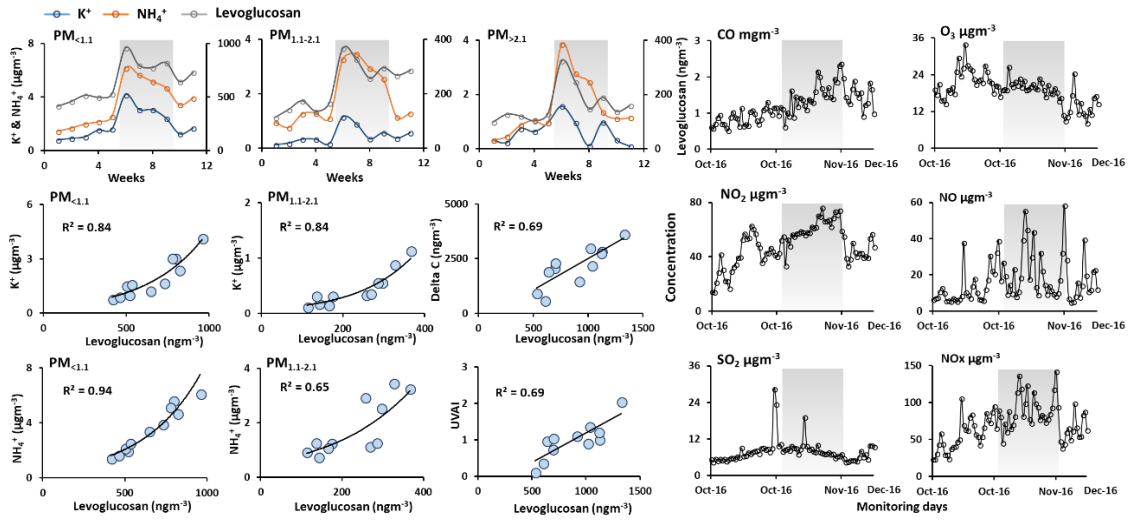**Note**. The blue and red shade in the graph at lower panel indicates the standard deviation.

7

8

1

Fig. 5. Size-segregated particulate bound (a) organic aerosols, and difference in the molecular compositions of (b) n-alkanes and (b) fatty acids.

1

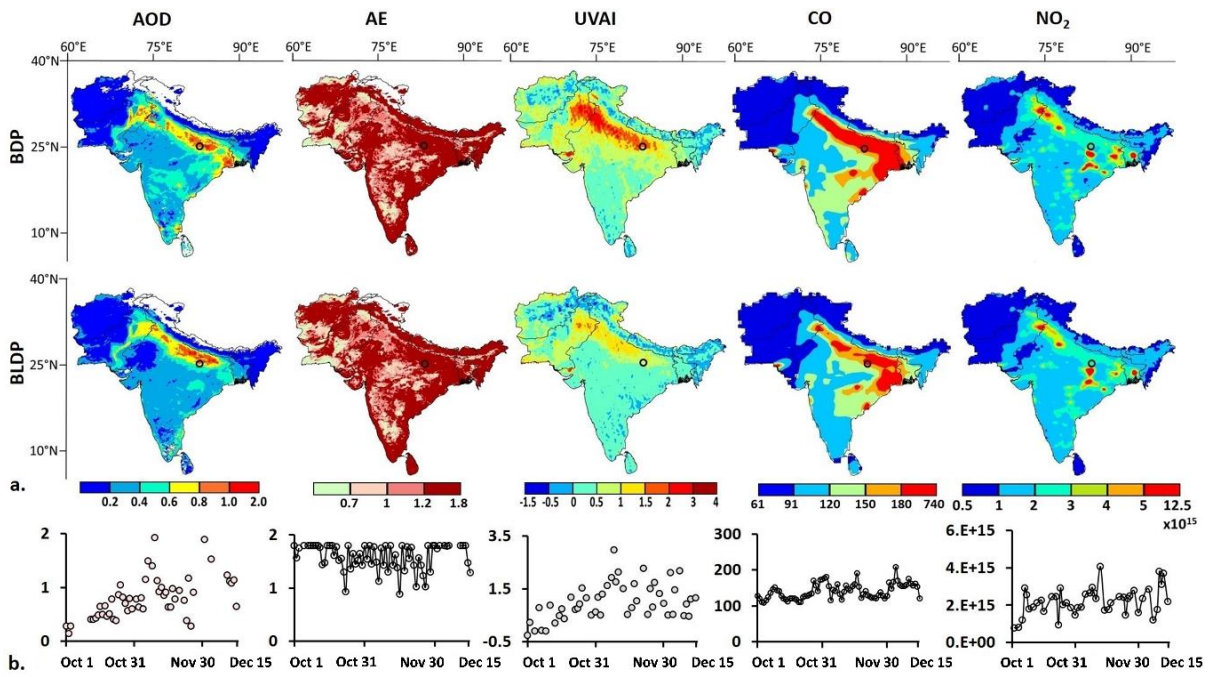Fig. 6. Temporal variation of trace gases and biomass burning signature molecules (NH$_4^+$, K$^+$, Levoglucosan), and their associations within different aerosol size fractions.

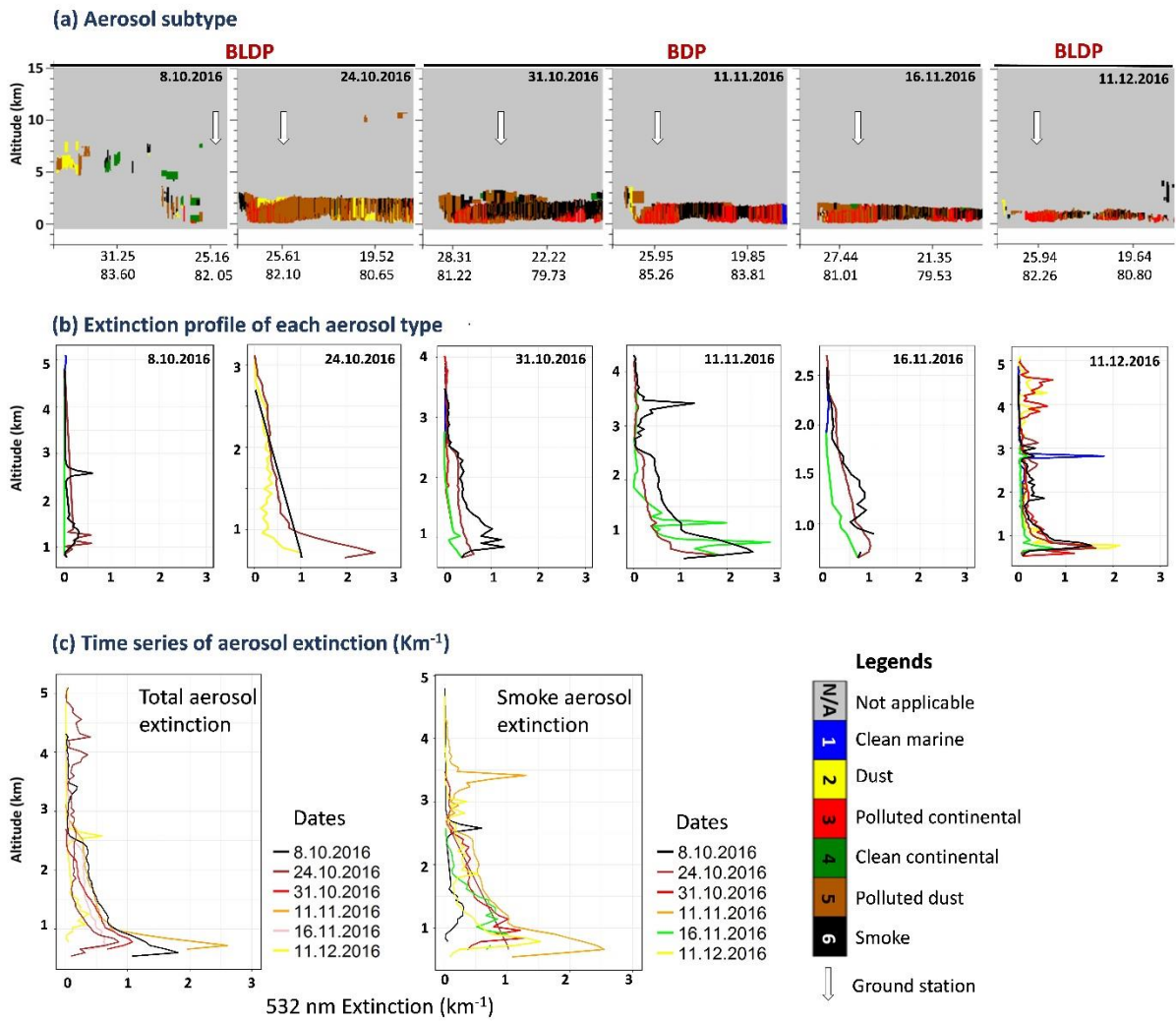**Note.** The shaded area indicates the peak biomass burning emissions.

1

Fig. 7. Episode specific spatial distribution of AOD, AE, UVAI, surface CO (ppbv) and tropospheric NO_2 (molecules cm^{-2}) over (a) South Asia and (b) at ground station.

Note. The lower panel indicates the time-series for each parameter retrieved particularly over the ground station.

(a) Aerosol subtype

BLDP   BDP   BLDP

8.10.2016   24.10.2016   31.10.2016   11.11.2016   16.11.2016   11.12.2016

31.25   25.16   25.61   19.52   28.31   22.22   25.95   19.85   27.44   21.35   25.94   19.64
83.60   82.05   82.10   80.65   81.22   79.73   85.26   83.81   81.01   79.53   82.26   80.80

(b) Extinction profile of each aerosol type

8.10.2016   24.10.2016   31.10.2016   11.11.2016   16.11.2016   11.12.2016

(c) Time series of aerosol extinction (Km^{-1})

Total aerosol extinction

Dates
— 8.10.2016
— 24.10.2016
— 31.10.2016
— 11.11.2016
— 16.11.2016
— 11.12.2016

Smoke aerosol extinction

Dates
— 8.10.2016
— 24.10.2016
— 31.10.2016
— 11.11.2016
— 16.11.2016
— 11.12.2016

532 nm Extinction (km^{-1})

Legends

N/A Not applicable
1   Clean marine
2   Dust
3   Polluted continental
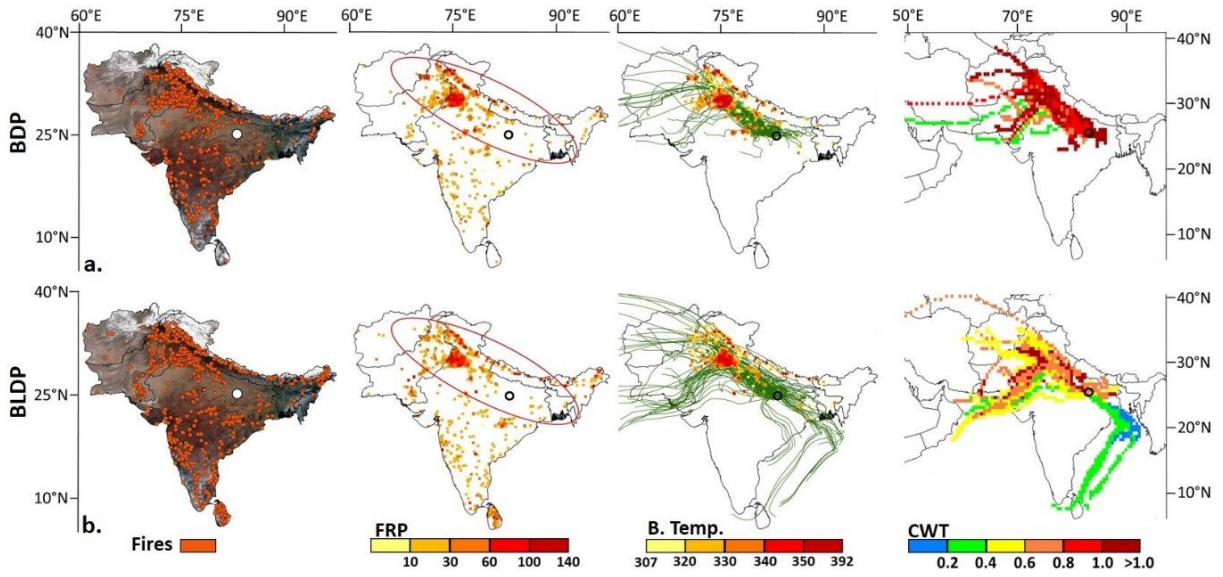4   Clean continental
5   Polluted dust
6   Smoke
⇩   Ground station

Fig. 8. Aerosol vertical profiles from selected CALIPSO overpasses across ground station (a) aerosol subtypes, (b) extinction coefficients of each aerosol type and (c) time series of extinction profile for total and smoke aerosols.
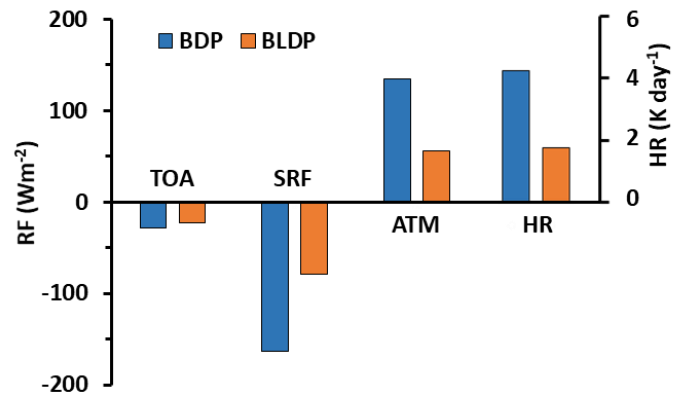
1

2
3

Fig. 9. Episode specific MODIS fire count, fire radiative power (FRP, MW), brightness temperature (B. Temp., K), and five days air mass back-trajectory along with CWT.

6
7

1

2
3
4   Fig. 10. Episode specific aerosol short wave radiative forcing and atmospheric heating.
5
6